UC San Diego

UC San Diego Electronic Theses and Dissertations

Title

Development of Models to Describe the Electrical Properties of Cardiomyocytes

Permalink

https://escholarship.org/uc/item/6pm0v4wm

Author

Lombardo, Daniel

Publication Date

2018

Peer reviewed|Thesis/dissertation

eScholarship.org Powered by the California Digital Library
University of California

UNIVERSITY OF CALIFORNIA SAN DIEGO

Development of Models To Describe the Electrical Properties of Cardiomyocytes

A dissertation submitted in partial satisfaction of the
requirements for the degree
Doctor of Philosophy

in

Physics

by

Daniel Marcus Lombardo

Committee in charge:

Wouter-Jan Rappel, Chair
Olga Dudko
Elena Koslover
Andrew McCulloch
Oleg Shpyrko

2018

Copyright
Daniel Marcus Lombardo, 2018
All rights reserved.

The dissertation of Daniel Marcus Lombardo is approved, and it is acceptable in quality and form for publication on microfilm and electronically:

_____

_____

_____

_____

_____

Chair

University of California San Diego

2018

DEDICATION

EPIGRAPH

Far and away the best prize that life has to offer

is the chance to work hard at work worth doing

—Theodore Roosevelt

TABLE OF CONTENTS

LIST OF FIGURES

LIST OF TABLES

ACKNOWLEDGEMENTS

I would like to thank my advisor, Wouter-Jan Rappel, for his support and guidance throughout the years. I would also like to thank my committee members for their assistance and constructive feedback. I'm truly grateful for all the help I have received from them.

Chapter 2, in full, with minor changes to formatting, is a reprint of the material as it appears in PLoS Computational Biology, 2016. Lombardo, Daniel; Fenton, Flavio; Narayan, Sanjiv; Rappel, Wouter-Jan. The dissertation/thesis author was the primary investigator and author of this paper.

Chapter 3, in full, with minor changes to formatting, is a reprint of the material as it appears in Chaos, 2017. Lombardo, Daniel; Rappel, Wouter-Jan. The dissertation/thesis author was the primary investigator and author of this paper.

Chapter 4, in full, with minor changes to formatting, has been submitted for publication of the material as it may appear in Physical Review Letters, 2018. Lombardo, Daniel; Rappel, Wouter-Jan. The dissertation/thesis author was the primary investigator and author of this paper.

VITA

2012	B. S. in Physics, suma cum laude, University of California Los Angeles
2012-2018	Graduate Teaching Assistant, University of California San Diego
2014	M. S. in Physics, University of California San Diego
2018	Ph. D. in Physics, University of California San Diego

PUBLICATIONS

Daniel Lombardo, FH Fenton, SM Narayan, W-J Rappel"Comparison of Detailed and Simplified Models of Human Atrial Myocytes to Recapitulate Patient Specific Properties", PLoS Computational Biology, 2016.

Daniel Lombardo, W-J Rappel, "Systematic Reduction of a Detailed Atrial Myocyte Model", Chaos, 2017.

ABSTRACT OF THE DISSERTATION

Development of Models To Describe the Electrical Properties of Cardiomyocytes

by

Daniel Marcus Lombardo

Doctor of Philosophy in Physics

University of California San Diego, 2018

Wouter-Jan Rappel, Chair

The membrane electric potential of the human heart depends on numerous of ionic channels and concentrations. Spikes in the membrane potential are responsible for the contracting of the heart, but disruptions to the membrane potential are also responsible for disorders. A cardiac arrhythmia is an irregular heartbeat that is caused by an abnormal activation pattern in the membrane potential. This dissertation focuses on the development of computational models that describe the membrane potential, and examines the conditions for when an arrhythmia can occur. We begin by comparing the efficacy of a highly detailed model, and a very simple one, to describe patient specific quantities of the membrane potential. From this we conclude that increased complexity does not improve the model's ability to describe the data. Next, we use

a unique approach of reducing a detailed model in order to develop our own simplified model. In this way we remove the variables and equations that are not necessary, while still preserving physical relevance for the parameters that are most essential to describing the voltage. Finally, we examine the spiral wave dynamics typically seen in cardiac systems, and look to understand when these spirals can become chaotic. Surprisingly, a single spiral can become chaotic without breaking up into multiple waves. Together these results offer new insights into the physics of cardiac dynamics, and present new possibilities for future treatment of cardiac arrhythmias.

Chapter 1

Introduction

The heart is a complex organ that pumps blood throughout the body, and is vital for nearly all living things. The human heart consists of four main chambers: the left and right atria, and the left and right ventricles. As the atria fill with blood the muscles on the heart begin to contract, forcing the blood down into the ventricles. The ventricles then contract and push the blood out into the arteries. The process of contraction is driven by an electrical signal that propagates along the walls of the heart. Ideally, the electrical signal begins at the sinoatrial node in the right atria, and travels down into the ventricles via the ventricular septum. However, defects in the cardiac tissue can cause this signal to be disrupted, and thus make the heartbeat irregular. This dissertation focuses on computational models of this electrical signal, and the irregular patterns that it can generate. We first give a brief overview of the models, along with the motivation behind the specific topics presented in later chapters.

The electrical signal propagates throughout the heart muscle via diffusion and active transport. Each cardiac cell has a series of channels which allow certain ions to pass through the membrane (namely sodium, calcium, and potassium). These channels do not remain open at all times, and therefore there is a potential difference between the outside and inside of the cell. The cells inherently have a negative membrane potential while at rest (approx. -70mV), but in

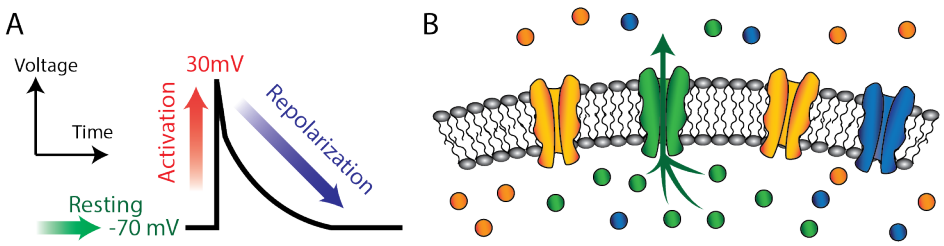

Figure 1.1: A: An example of the spiking pattern seen in cardiac cells, known as an action potential. B: a visual representation of the cell membrane with ion channels. Many of the channels in cardiac cells are voltage gates, and only open when the membrane potential crosses a certain threshold. Thus, not all the channels are active at the same time.

the presence of an electrical stimulus it can quickly spike upwards. The potential then slowly returns to its resting state over time. The spiking of the membrane voltage is known as an action potential, and is shown in Figure 1.1. As this process is responsible for the contractions of the heart, any disorders or disruptions in the electrical signal can easily become fatal. Hence, there is strong motivation to understand the underlying dynamics of the action potential.

Arrhythmias are irregular heart beats that can be caused by a variety of factors. For instance, inhomogeneities in the cardiac tissue or changes in the pacing frequency can cause the electrical signal to be disrupted and lead to an arrhythmia. This can be temporary in some cases, or long term and even fatal. In the extreme cases, the arrhythmia is more than an irregular beat and actually causes the entire contraction of the heart muscle to stop. Fibrillation, a type of arrhythmia, is the process of when the heart is no longer beating, but rather ”quivering” rapidly. This prevents the blood from properly pumping and can quickly become fatal. This can occur either in the ventricles or in the atria. Clinical treatment of arrhythmias is still limited, and overall has a low success rate. One of the main difficulties in developing better treatment options is that our understanding of the human heart remains limited. While studies can be done on various animal hearts, these do not reproduce all the features of the human heart.

Studying the electrical signal of the heart, particularly in humans, is extremely challenging. Electrocardiograms (EKG's) are one of the most common methods used, but offer limited insight. The procedure involves the placement of electrodes on the surface of the skin that measure average

changes in the electrical signal over time. However, this approach is mainly used for recording the heart beat, and provides limited information about the action potential itself. Furthermore it primarily provides an average of the entire heart, or a large area of it, with little information for localized regions.

In vitro studies have been done on animal hearts, usually mice, that can offer more insight. Optical mapping with voltage sensitive dyes can even be used to record the action potential in a local region of the heart. This technique can be used to study the wave front, and activation pattern of the electrical signal as it propagates along the surface of the heart. Yet there is some debate as to how similar in vitro studies are to in vivo. There is also the drawback that these techniques cannot be applied to human patients.

Finally, there are some methods for studying the action potential of a human heart. The technique that is most relevant to this thesis is the basket catheter approach. This involves inserting a long catheter into the patient with a flexible ”basket” on the end that contains a series of electrodes. Once the catheter has reached the interior of the heart, the basket can be expanded so that each of the electrodes touches the surface of the heart. This allows for numerous, localized measurements of the membrane voltage. With enough electrodes in contact with the surface of the heart, this method can also be used to study the wavefront and activation pattern of the signal. The issue is that this type of study is usually only done on patients with a cardiac disorder. Thus limiting both the breadth and size of the data available, as there are a limited number of potential patients.

Simulations generated by computers are often an effective way to study the dynamics of cardiac cells, and will be the focus of this thesis. While we discuss the membrane potential here, it is worth mentioning that simulations can be used to study a wide variety of problems in the heart. For instance, there are many models that examine the mechanics and consequences of stress and strain in heart. Pharmacological studies also use simulations to study to predict the effects of certain drugs on the ion channels and overall performance of the heart.

1.1 Motivation

While there are many readily available models for the membrane potential of the heart, they have rarely been studied in the context of actual human patient data. As mentioned previously, obtaining accurate data with human patients can be very challenging, and thus many models have been designed using data from other species. By pulling from different species, and different data sets, computational models of the heart have become highly detailed. Yet there remains little to no understand as to how well these models can describe human data sets. This understanding is crucial if simulations are to aid in clinical treatment. The growth in complexity with cardiac models also presents another problem. The increase in detail leads to an increase in computational cost, and a decrease in intuition about the model parameters. If a model is too complex, it loses it's effectiveness at describing a given data set. Issues such as over-fitting, and lack of computational resources, begin to appear. Furthermore, many simulations do not examine a single cell, but rather a network of cardiac cells. In this case the problems only get worse, as it becomes harder to gain any insight from the model. It is then the focus of this thesis to address these issues.

In Chapter 2, we examine two established models of the membrane potential for a cardiac cell. One is a very detailed, electrophysiological accurate model, with over forty time dependent variables and many more parameters. The other is a much simpler model, with only four time dependent variables and approximately twenty parameters. We examine how well each of these models can describe data from human patients provided in collaboration with the Veteran's Hospital at UCSD. We fit each of the models to patient specific data and compare the results. Interestingly, the simplified model performs just as well as the detailed model. Thus showing that while detailed models certainly can provide more information, they are not always better at describing the data. This study is particularly important in improving patient specific modeling. If simpler models can be used to describe the data, then studying the dynamics of individual patients becomes much more computationally feasible.

The main drawback of the simple model used in Chapter 2, is that its variables and parameters do not have any physical meaning. The model was designed to reproduce characteristics of the membrane voltage, not to accurately describe the actual channels or concentrations in the cell. This is a common issue in models of the membrane potential, in which physiologically relevant parameters only come with highly detailed models. In Chapter 3, we then develop a simple model that reproduces many of the same characteristics while also maintaining electrophysiologically meaningful parameters. We start with a very detailed model, and use a reduction algorithm to remove and simplify the equations of the model that are not necessary for describing the membrane voltage.

Another pressing issue with cardiac models is the complexity and cost of simulations of extended domains. While performing a simulation for the membrane potential of a single cell is relatively simple, studying the waves and activation patterns of the heart requires simulations of several thousands of elements simultaneously. Furthermore, it is often challenging to directly relate model parameters to the dynamics observed over extended domains. There are many interesting wave patterns that can develop for excitable media, but not much is known about the underlying dynamics of these waves. Of particular interest in cardiac dynamics is the formation of spiral waves, which are believed to be connected with cardiac arrhythmias. Chapter 4 then looks in more detail at these dynamics of two-dimensional simulations. There we will examine the different spiral wave trajectories that are possible, along with the conditions for when these trajectories can become chaotic.

Yet before going into the details of the problems described above, we first present a general overview of the basis for computational models in the heart that will be used.

1.2 Action Potentials

The action potential for cardiac cells, as shown in Figure 1.1A, can be broken up into several key regions. There is the initial, rapid depolarization in which the membrane potential quickly rises. After this initial jump, the potential will slowly decrease, and could even plateau. This can last on the order of 100ms. Finally, the potential rapidly drops back down to the resting state. There are a variety of factors that can affect how long each of these phases take, and what values the membrane potential can range over.

Throughout this thesis, in order to quantify the differences in action potentials, we use three standard metrics. We first consider the overall shape of the action potential. While all action potentials follow the general pattern discussed above, there can be noticeable differences. Next is the action potential duration (APD), which defines how long it takes for the cell to decay back to its resting state after a stimulus. The APD90 is the time from the peak of the action potential to the point where it has decayed back to 90% of its resting state value. It is usually difficult to find an absolute end to the action potential, particularly in human patient data, so 90% repolarized is easier to find than 100%.. The third quantity considered is the conduction velocity (CV), which represents how quickly the action potential travels between cells. For human patients, this tends to be 50-100cm/s. For the purposes of this thesis, we will take the assumption that all tissue is isotropic. However it is important to realize that the velocity can vary depending on the region of the heart, and the direction of the wave.

It also important to consider how these three quantities change with the pacing of the cell. The time between stimuli can greatly affect the shape, APD, and CV of the cell. To help quantify this change, we define the diastolic interval (DI) as the time from 90% repolarization of the *last* stimulus to the beginning of the *current* stimulus. Figure 1.2 shows a representation of the DI and APD ranges. Both the APD and CV will usually decrease as the DI gets smaller, and begin to level out at higher DI values.

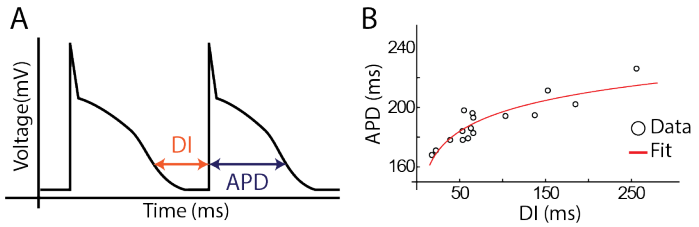

Figure 1.2: A: A visual representation of how the diastolic interval (DI) and action potential duration (APD) are defined. B: An example of a plot showing how the APD changes as a function of DI.

It is important to note what happens as we continue to lower the value of the DI. While the APD and CV continue to shrink, we eventually reach a cut-off at which the cell no longer experiences an excitation. Meaning that after every excitation of the cell, there is a window of time for which it ignores any other stimuli. Depending on the shape of the APD vs DI curve this can lead to a variety of situations, but in general the activation pattern will become irregular. Therefore the contraction of the heart also becomes irregular. It is then crucial that we understand more about what situations can cause irregular activation, and what the possible outcomes are.

1.3 Cable Theory

Cable theory is the basis for nearly all cardiac models of the membrane potential. Principally, it is the idea that a long line of cells can be treated as an electrical cable. The overall design was first proposed by William Thomson [Tho56b, Tho56a], and later shown by Weidmann [Sil52] to be applicable to the electrical signal in the heart. The concept can also be extended to two or three dimensions, where the cable becomes more like a grid or mesh. For now, we shall only consider the one dimensional case. The basic idea is that the membrane potential of the cell can be modeled by treating the membrane as a series of resistors and capacitors. Furthermore, interactions between neighboring cells are defined by a resistance per unit length r_a in between each cell. Figure 1.3 shows the basic design.

Cable theory was originally applied to the axon of a neuron. In this case the current

flows through the axon with some resistance per unit length r_a. Current then escapes through the membrane, which also has a resistance and capacitance per unit length of r_m and c_m respectively. Here we consider cardiac cells, which are more discrete. Each cardiac cell has its own membrane, yet the membrane potential still spreads into neighboring cells by diffusion. This is because there exists a gap junction between neighboring cells, which allow ions to flow between the intracellular regions of neighboring cells. If we consider a long, one-dimensional line of cells, the gap junctions effectively combine all the cells into one continuous cable [PB88, CHA95]. This approximation allows us to apply the cable equation to systems of cardiac cells.

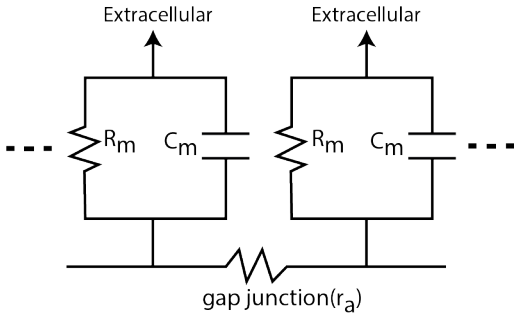

Figure 1.3: Diagram showing the main components of the membrane potential modeled as an electrical cable. R_m and C_m are the resistance and capacitance of the membrane respectively. The resistance of the membrane represents the ionic channels. r_a is the resistance per unit length in between the cells.

In order to find an equation of the membrane voltage, we first consider the various currents. Each element, or cell, is connected by a wire with some resistance per unit length r_a. When a current I_a is applied to the cable, it induces a change in the voltage described by Ohm's Law. The difference in voltage between two neighboring cells separated by a distance Δx is given by

$$\Delta V = -I_a r_a \Delta x \tag{1.1}$$

The negative sign comes from the voltage decreasing over the length of the cable. When

the spatial distance becomes very small, we can rewrite the equation as

$$I_a = -\frac{1}{r_a}\frac{\partial V}{\partial x} \tag{1.2}$$

This relation can then be related to the current in the membrane using Kirchhoff's Laws. As the current passes through the cable it is split at each cell, where some current goes into the membrane and the rest goes to the next cell. This gives the following relation:

$$I_a(x) = I_a(x+\Delta x) + \Delta x(I_C + I_R) \tag{1.3}$$

Again, taking Δx to be a small value gives

$$-\frac{\Delta I_a}{\Delta x} = I_C + I_R \tag{1.4}$$

By using the relations between the voltage and the currents, this expression can be rewritten as

$$\frac{1}{r_a}\frac{\partial^2 V}{\partial x^2} = c_m\frac{\partial V}{\partial t} + I_R \tag{1.5}$$

As stated before, the current through the membrane is given by the resistor component in the RC circuit. If there are multiple currents, then we just need to add more resistors, each with current i_j to the circuit.

$$\frac{\partial V}{\partial t} = \frac{1}{r_a c_m}\frac{\partial^2 V}{\partial x^2} - \frac{1}{c_m}\Sigma_j i_j \tag{1.6}$$

Typically, the resistance in the membrane channels is not a constant, but actually changes with the ratio of ions inside and outside the cells. Physically, this is explained through the Nernst potentials for the relevant ions. The channels do not remain open at all times and can close when a threshold is reached. Complex, detailed, models of the heart therefore include equations to

model the ionic concentrations within the cells. Furthermore, some models include the effects of the sarcoplasmic reticulum on the ionic concentration. As mentioned before, a comparison of a detailed and simplified model for one-dimensional simulations is given in Chapter 2. A thorough analysis of which ionic currents contribute the most to the action potential is shown in Chapter 3.

When extending this type of model to two or three dimensions the diffusion term $\frac{\partial^2 V}{\partial x^2}$ must expand to account for the new directions. The cable then becomes a mesh. While this greatly increases the complexity and computational cost of the model, it also creates new, interesting, behaviors as well.

1.4 Modeling Membrane Current

A crucial component in the work presented here is then the mathematical model that describes the ion channels of the membrane. Numerous models have already been developed to characterize this system, many of them building on the work of previous ones. The models vary from detailed, with numerous components, to simplified with a minimal set of variables. While the cable equation discussed above shows the overall structure for many of these models, the details of the resistance terms can vary significantly.

First, it should be pointed out that there is no single model that describes the entire heart. There are models that have been designed to describe atrial tissue, and others that describe ventricular tissue. Furthermore there are models specifically based on a certain species, such as a model of the rabbit heart. In this thesis, we focus on generic models of the atrial membrane potential. These models are similar in design to ventricular models, but vary slightly in the parameters. Thus, many of the current equations and general concepts discussed here apply to a variety of other models as well.

One of the first models designed specifically for describing cardiac cells was developed by Noble in 1962 [Nob]. It is based on the Hodgkin-Huxley model for the giant squid axon, and

includes three membrane currents shown below.

$$I_{Na} = g_{Na}(V_m - E_{Na}) \tag{1.7}$$

$$I_K = g_K(V_m - E_K) \tag{1.8}$$

$$I_{leak} = g_{leak}(V_m - E_{leak}) \tag{1.9}$$

The membrane potential is given by V_m. The currents I_{Na} and I_K represent the sodium and potassium ion channels respectively. The leakage current represents a small amount of charge that escapes through the membrane. Physically, for this model, it is attributed to chlorine ions. The parameter g in each cases represents the conductance of the channel. This design of the current equations, which once again makes use of Ohm's Law, is typical for many models of cardiac cells. The conductance for the individual channels can be constant, or a function of the membrane voltage.

The parameters E_{Na}, E_K, and E_{leak} are the equilibrium, or reversal potentials of the channels. In early models, these parameters were usually fixed to constant values, determined by fitting the model to experimental data. In modern, detailed models these values are defined by the Nernst equation.

$$E = -\frac{RT}{F}\log\frac{c_b}{c_a} \tag{1.10}$$

The concentrations c_b and c_a are the concentrations outside and inside of the membrane, respectively, for ions related to the given channel. For instance, E_K will depend on the concentration of the potassium ions inside and outside of the cell.

In recent years, cardiac models have become increasing complex and detailed. In this thesis, the model developed by Koivumaki, Korhonen, and Tavi in 2011 [KKT11] includes thirteen membrane currents. It also accounts for the uptake of calcium ions by the sarcoplasmic

reticulum, and the diffusion of sodium and potassium ions within the cell.

Yet this increased complexity presents several problems. The first is a large increase to computational cost. With many of the equations being nonlinear, it becomes necessary to use numerical differentiation and integration techniques. These simulations can take hours, or even days, to complete depending on the number of cells being simulated. The second issue is that while the models have grown the available data in human patients remains limited. Many of the recently developed models rely on data from a variety of different animal species to account for all the different channels and ions. Yet this data is not measured in every study, particularly with human patients. So there is an issue of the model over-fitting to the data. Of course, these issues only increase as simulations progress to higher dimensional spaces.

1.5 Two-Dimensional Simulations and Spiral Waves

As discussed previously, the propagation of the action potential causes the heart to contract. A stimulus originating in the atria will cause an electrical wave to propagate outward, and eventually into the ventricles. The contraction of the heart follows this wave. In reality, the wave propagates along the surface of the heart, and through the walls as well, making it three dimensional. However, the atria are relatively thin, making two-dimensional models a good approximation.

A two-dimensional system of excitable media is capable of generating a variety of waves. For instance, a stimulus that is applied to a single point will propagate radially outward. A stimulus that is applied to a thin strip will create a plane wave. Ideally, the electrical wave propagates in a clean, uniform fashion across the surface of the heart, from the atria down to the ventricles. However, there are many instances where this signal can become disrupted and lead to an arrhythmia. If severe enough, an arrhythmia can lead to cardiac arrest and become fatal.

In particular, it is known that the likely cause of an arrhythmia is when the membrane

potential wave becomes a spiral [GEKS92, GPJ98, NKS+12, NKR12, NKER12]. Figure 1.4 shows a of snapshots that demonstrate this in a simulation. Spiral waves can form under a variety of conditions, such as when multiple waves collide with each other or when part of the tissue becomes nonconducting. Yet studying these wave dynamics in human patients is extremely difficult to do. In order to collect data on spiral waves it is necessary to have multiple electrodes recording from the surface of the heart. However the resolution of the wave is only as good as the spacing between the electrodes. In practice, spiral waves have been observed in human patients, but accurately tracking the spiral over time can be extremely difficult. Simulations are once again a very attractive choice for studying these waves.

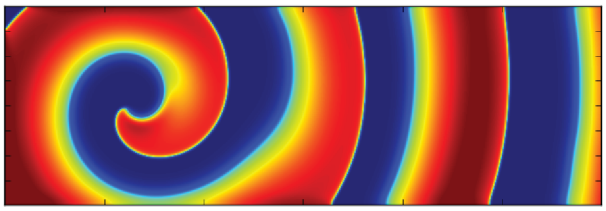

Figure 1.4: Snapshot of a spiral created during a simulation of the Fenton-Karma model [FCHE02], which is based on the cable theory discussed above. The membrane potential of individual cells is given the color map, which ranges from blue (resting state) to red (depolarized).

It is also worth noting that not every cell or element in the simulation needs to be identical. Actual data of tissue or medium will likely be inhomogeneous to some degree. It is therefore important to be able to include this in simulations. For the models described in this dissertation, and in particular Chapter 4, inhomogeneities are simulated by adjusting the parameters of the membrane current. By changing these parameters in local regions of the simulated tissue, we create heterogeneities that can affect the trajectory of waves.

While this thesis focuses on two-dimensional waves, it is also possible to perform three-dimensional simulations as well. In this case, the wave propagates along the surface and through the walls of the heart. Instead of spiral wave, these are known as scroll waves. While scroll waves are physically more accurate, the computational cost for simulations can be exceedingly high. Considering that modern models have approximately 40 nonlinear differential equations, with a

grid size of 100x100x100 elements we would have $4 * 10^7$ equations to solve for every time step!

Chapter 2

Comparison of Detailed and Simplified Models of Human Atrial Myocytes To Recapitulate Patient Specific Properties

2.1 Abstract

Computer studies are often used to study mechanisms of cardiac arrhythmias, including atrial fibrillation (AF). A crucial component in these studies is the electrophysiological model that describes the membrane potential of myocytes. The models vary from detailed, describing numerous ion channels, to simplified, grouping ionic channels into a minimal set of variables. The parameters of these models, however, are determined across different experiments in varied species. Furthermore, a single set of parameters may not describe variations across patients, and models have rarely been shown to recapitulate critical features of AF in a given patient. In this study we develop physiologically accurate computational human atrial models by fitting parameters of a detailed and of a simplified model to clinical data for five patients undergoing ablation therapy. Parameters were simultaneously fitted to action potential (AP) morphology,

action potential duration (APD) restitution and conduction velocity (CV) restitution curves in these patients. For both models, our fitting procedure generated parameter sets that accurately reproduced clinical data, but differed markedly from published sets and between patients, emphasizing the need for patient-specific adjustment. Both models produced two-dimensional spiral wave dynamics for that were similar for each patient. These results show that simplified, computationally efficient models are an attractive choice for simulations of human atrial electrophysiology in spatially extended domains. This study motivates the development and validation of patient-specific model-based mechanistic studies to target therapy.

2.2 Introduction

Atrial fibrillation (AF) is the most common sustained cardiac arrhythmia and is associated with increased morbidity and mortality from stroke and heart failure [CHN$^+$13]. Unfortunately, therapy for this condition is suboptimal due to its mechanistic complexity [Nat02, Jal11]. Because of difficulties in studying AF mechanisms in humans, and since animal models of AF may differ from human AF, mechanistic studies of arrhythmias are increasingly turning to computational modeling to bridge the gap between clinical unmet needs and cellular studies. Essential in these computational studies is the choice of the electrophysiological model which simulates the membrane potential through a set of parameterized equations that describe the ion channels. This model can range in complexity from detailed [CRN98, NFF$^+$98, MGTG08, KKT11, GPV$^+$11], which describe as many channels as possible, to simplified [FK98, Kar94, KKB$^+$91], which capture only essential dynamical features of cardiac tissue. However, these computational models are rarely validated in humans, and their parameters are typically based on imprecise, incomplete, or animal data. We set out to address this problem by developing computational models that recapitulate cellular and tissue behavior in human AF. We used three sets of clinically obtained data from the left atria in 5 different patients with clinical AF at invasive electrophysiological studies. The data included action potential (AP) morphology, excluding the upstroke due to pacing artifacts, AP duration (APD), and conduction velocity (CV) restitution curves obtained during controlled pacing using a monophasic action potential (MAP) catheter, and maps of AF propagation obtained from direct contact wide-area multipolar basket catheters [NKR12]. We used a simulated annealing fitting procedure to adjust the model parameters such that the numerical results fit the AP morphology and the restitution curves simultaneously. This was done first for the detailed Koivumki et al (KKT) atrial myocyte model [KKT11] which extends earlier detailed models [NFF$^+$98, MGTG08] to account for Ca2+ dynamics in the sarcoplasmic reticulum. We show that our fitting procedure was able to generate parameter sets that accurately

reproduce clinical data. These sets differ significantly between patients and are markedly different than the published one. We then fitted the clinical restitution curves and the full AP morphology obtained from the KKT model (i.e., including the upstroke) to the simpler Fenton-Karma (FK) model [FK98]. We show that we are able to obtain parameters that can reproduce the clinical data and the fitted AP morphology well. Of note, a modeling sequence in which the FK model is fitted to clinical data, followed by a KKT fit to the FK output is equally possible. Finally, we simulated spiral wave reentry in two-dimensional sheets using the fitted parameters sets for both models in all patients. We find that the dynamics of the spiral waves are similar for each patient. This suggests that simplified, computationally efficient models can be used to investigate spatio-temporal dynamics of cardiac activation. Our study shows how numerical models can be tailored to patient-specific clinical data, an important step towards guiding therapy based on individual AF mechanisms.

2.3 Methods

Detailed Methods are available in Appendix A.

2.3.1 Clinical Mapping

We acquired data from 5 patients with atrial fibrillation undergoing ablation for standard clinical indications, of age 64.210.6 years, left atrial diameter 423 mm and left ventricular ejection fraction 6010%. All patients were studied after discontinuing all anti-arrhythmic medications for over 5 half-lives (amiodarone in 1 patient was discontinued 1 year earlier). MAPs were recorded during incremental pacing from slow heart rates to AF onset[NFC$^+$11]. In brief, a deflectable 7F MAP catheter (EP Technologies, Sunnyvale, CA) was advanced to record AP in the antra of the right and left superior pulmonary veins. The protocol was completed before ablation. Patients in AF were electrically cardioverted to yield sinus rhythm, and the protocol started 10 minutes later.

APs were recorded from distal poles of the MAP catheter while pacing the proximal poles. The close proximity of the recording and pacing poles necessitated special treatment for the first 30 ms of each AP morphology, as detailed in Appendix A. The resulting AP morphology captures repolarization but does not include the upstroke. We paced for ¿84 beats at each cycle length (CL) of 500 (baseline), 450, 400, 350, and 300 ms, then in 10 ms steps to AF or capture failure, whichever came first. Further details regarding signal processing, APD, and how activation time data was used to determine CV can be found in the Appendix.

2.3.2 Numerical Simulations

Simulations were carried out using the monodomain equation:

$$\frac{du}{dt} = D^2u - I_ion/C_m. \tag{2.1}$$

where u is the membrane voltage, Cm represents the membrane capacitance, D is the diffusion coefficient (1D) or isotropic tensor (2D) and Iion represents the membrane currents. Simulations in our fitting procedure were carried out in homogeneous 1D cables, consisting of 100 elements with a spatial discretization of 0.02 cm and a time step of 0.01 ms using no-flux boundary conditions. Decreasing the time step to 0.005 ms adjusted the CV restitution values by less than 4.5% for the FK model, and less than 1.5% for the KKT model while decreasing the spatial discretization to 0.01 cm changed these values by less than 7%. For the 2D simulations, we solved the monodomain equations in isotropic sheets of at least 9.6x9.6 cm using a square computational grid, again with a spatial discretization of 0.02 cm and a time step of 0.01 ms using an explicit Euler method. Spiral wave reentry was generated through cross-activation and spiral tip trajectories were computed using a previously published algorithm [FK98]. It is also important to note that while all simulations were carried out with isotropic tissue, actual tissue is heterogeneous. Including tissue anisotropy would require more detailed data on tissue

conduction and fiber orientation. Computations were performed using the C++ language and MPI parallelization on a high-performance workstation consisting of dual quad-core Xeon E5-2637 CPUs. Typical fitting simulations starting with the published parameters as initial conditions consisted of 50 iterations and required approximately 6 CPU hours for the FK model and 32 hours for the KKT model. This time can be significantly reduced if the initial parameter values are close to the final results. For instance, if two patients have similar dynamics, then the fitted parameters for one can be used as the starting point for the other. 2D simulations were performed on a GPU parallel computing platform with a Nvidia Tesla K40 graphics card. Computing 1000 ms of spiral wave propagation on a 512x512 grid required approximately 8 min for the FK model and 37 min for the KKT model.

2.3.3 Electrophysiological Models

In this study, we employed a version of the FK model which consists of four variables, three gating variables and the membrane potential, and 24 parameters [CENF07]. Three of these parameters were fixed (see Appendix A), resulting in 21 adjustable parameters. The KKT model consists of 43 variables and more than 100 parameters [NFF$^+$98, KKT11] and, as described in the Appendix, fits were carried out by allowing 21 parameters to vary (S1 Table). When shifted 50% away from their original published values, each of these parameters was found to increase the error by 1 to 65%. Here, error is quantified as specified in Appendix A. Many of these parameters were shifted by even larger amounts in the final fits.

2.3.4 Curve-fitting Procedure

We used a simulated annealing fitting procedure in which parameter values are repeatedly adjusted in an attempt to minimize error functions which compare the numerical results to the clinical data set (see S1 Text). Unlike other algorithms, simulated annealing samples a large

region of parameter space and does not automatically reject parameter choices that do not improve the fit [PTVF07]. This is done by assigning an artificial temperature which determines the amount of variation of parameters for each iteration and is slowly reduced during the fitting procedure [PTVF07]. Note that this temperature is a variable of the fitting procedure, and is not related to any physiological value in the models or data. This algorithm has been successfully applied to biological data [TSA$^+$12, SYE$^+$14]. Simulations were started from a high temperature [SLR12] and typically consisted of 50 iterations after each of which we reduced the temperature by 10%.

2.4 Results

2.4.1 Clinical Data

In Fig 2.1A we show the clinically obtained AP morphologies for different CLs in one of the five patients, with voltage rescaled to span 0 and 1 and APD rescaled to 1 (raw APD90 ranged from 223-313 ms). Importantly, AP shapes are roughly independent of the CL, allowing us to define an average AP morphology for all CLs. This morphology, after the first 10 ms due the pacing artifacts has been removed, is shown in Fig 2.1B, together with its high-order polynomial fit (solid line). The resulting smooth AP morphology can then be used in the fitting procedure and can be adjusted to the required APD by a simple time dilation or contraction.

Fig 2.2 shows examples of APD and CV restitution curves used in our fitting study for one of our patients (#3). Fig 2.2A shows APD restitution as a function of diastolic interval (DI) from the MAP data (symbols) along with a logarithmic fit (S1 text). The clinical data relating CV and CL for the same patient, together with the polynomial fit, is shown in Fig 2.2B while in Fig 2.2C we have plotted the DI as a function of CL. The CV restitution curve based on the polynomial fit in Fig 2.2B and the dependence of DI on CL shown in Fig 2.2C is plotted in Fig 2.2D. The CV data for the remaining patients are shown in S1 Fig and S2 Fig.

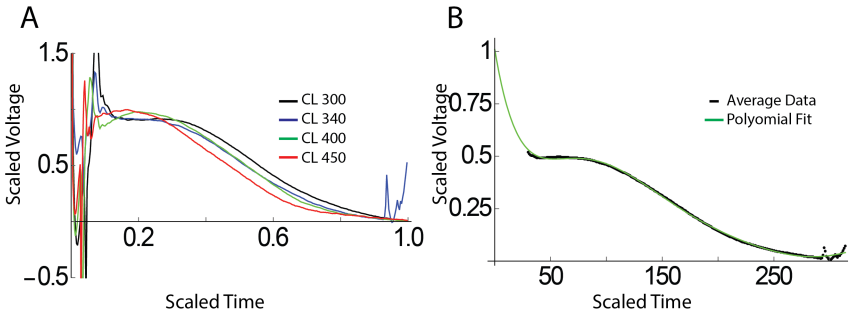

Figure 2.1: Determination of AP shape from clinical data. (A) MAP data in one of our patients (2) for different CLs (in ms). Time is rescaled and runs from 0 (stimulus) to 1 (repolarization). (B) Clinical data, corrected for pacing artifacts averaged over all CLs, shown as symbols and the corresponding polynomial fit.

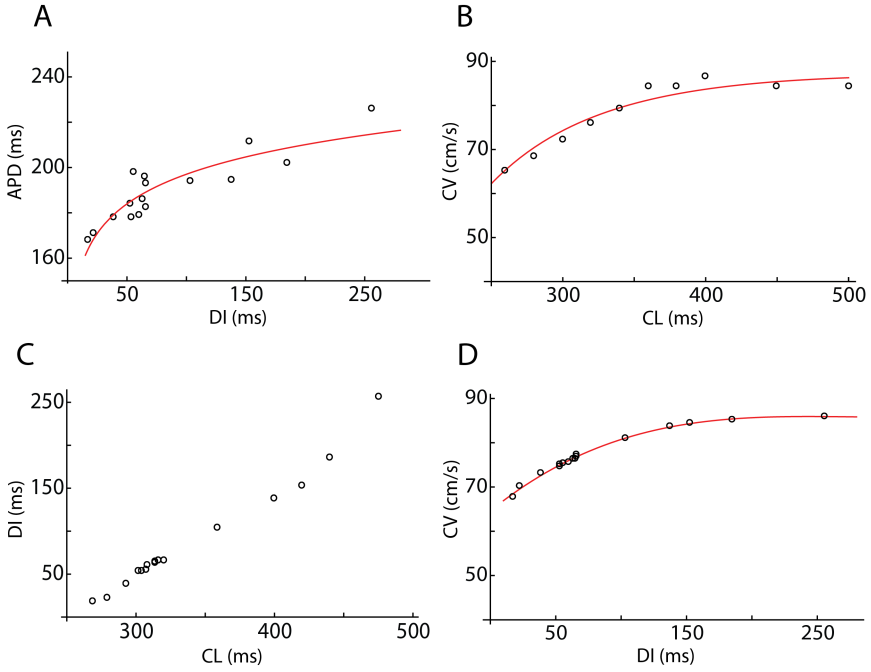

Figure 2.2: Clinical restitution data for patient 3. (A). The APD as a function of DI as determined from the MAP electrode (symbols) and the polynomial fit to the data (solid line). (B) DI as a function of CL from the MAP data. (C) CV as a function of CL using the activation times of the basket electrodes. (D) CV restitution curve computed using the data in (B) and (C). The symbols correspond to the values of the DI in (B).

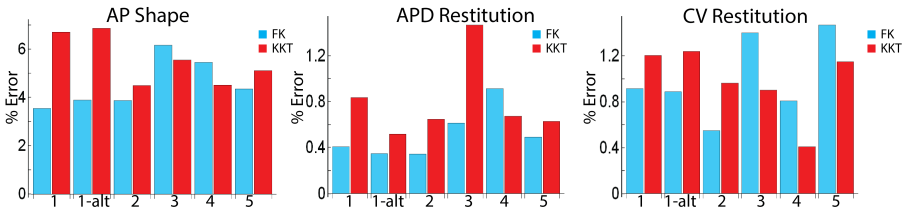

Figure 2.3: Error estimates of the obtained fits. The average error in both models is shown for the morphology, APD, and CV restitution curves for all patients, including the alternate parameter set for patient 1.

2.4.2 Parameter Fits

As discussed above, the clinical data does not incorporate information about the AP upstroke. This upstroke, however, is largely responsible for the wave front dynamics and a meaningful comparison of spatio-temporal dynamics between the results of the KKT and the FK model is only possible if the upstroke in both models is similar. To enable such a comparison, we chose to first fit the clinical data to the KKT model. The resulting AP morphology, now including the upstroke, and clinical restitution curves were then used as fitting input to the FK model. This fitting sequence ensures that, in the case of a successful fit, the AP upstroke in both models is similar. We have verified that switching the order of the fitting procedure did not change the computational times in a significant manner. For the KKT model, we fitted the parameters to the clinical data of the 5 patients. The resulting values of the five parameter sets are listed in S2 Table. The parameters for the FK model, fitted to the KKT output, can be found in S3 Table. For one of the patients, #1, we determined a second, alternate, set of parameters, by using different initial conditions for the parameter values. We quantified the accuracy of our fits by determining the average error for each fitted point (see Methods). A full summary of the results is shown in Fig 2.3, and discussed in more detail below.

For reference, the percent error for the original published parameters of each model was also quantified. The average percent error in AP shape ranged from 100% to 226% for the FK model, and from 10% to 24% for the KKT model. The APD restitution ranged from 26% to 37%

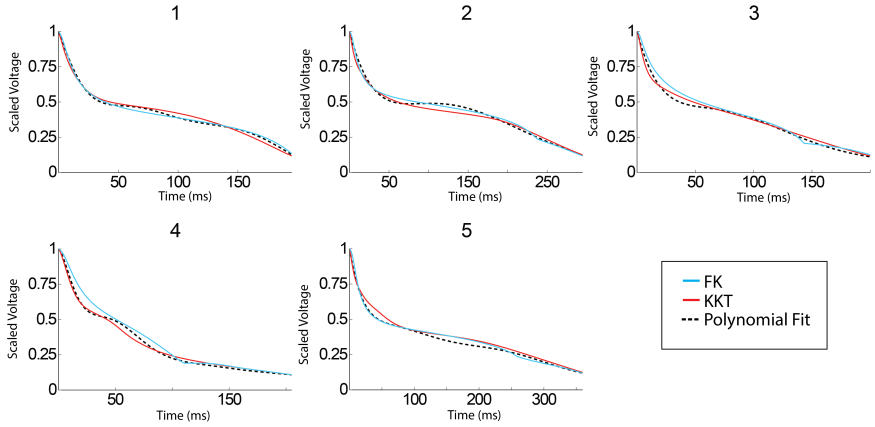

Figure 2.4: Clinical AP morphology compared to model AP morphologies obtained by fitting the model parameters. The average clinical AP morphology, corresponding to the largest DI value, is shown as a dashed line while the FK model is shown in blue and the KKT model is in red.

for the FK model, and 4.5% to 39% for the KKT model. The CV restitution ranged from 28% to 57% for the FK model, and 40% to 63% for the KKT model. We note that the original parameter set for the FK model was not chosen to describe atrial myocytes.

2.4.3 Action Potential Morphology

Fig 2.4 shows the AP morphology, corresponding to the largest DI value, obtained in all patients as dashed lines. Even though AP morphologies are similar, they differed in their precise shapes. The resulting morphologies from the KKT model, using parameters obtained from the fitting procedure, are shown in red. In this Figure, we show the shapes corresponding to the largest S2 stimulus (which differs for all patients) that was applied during the S1-S2 pacing protocol. Also shown in Fig 2.4, in blue, are the morphologies obtained by the FK model, fitted to the AP shapes from the KKT model.

A visual inspection reveals that both models can accurately reproduce the AP morphology for these patients. We quantified the accuracy of our fits by determining the average error for each fitted point (see Methods), and found that both models have a total error less than 6.8% when averaged over all S2s (Fig 2.3). The largest average error for a single S2 in the FK model was

11% (patient 4) while the largest error in the KKT model was 8% (patient 1). Furthermore, as shown in S3 Fig, the upstroke of the AP is similar between the KKT and FK models.

2.4.4 APD Restitution Curves

Fig 2.5 displays the polynomial fits to the clinically obtained APD restitution curves as gray symbols. Note that while the polynomial is a continuous function, only data points used for the model fits are shown. As expected, the general shape of this data is identical, with decreasing APD for decreasing DI [NKKR08]. The most noticeable difference between patients is the change in maximum APD values. While patient 1 only reaches to approximately 220 ms, the maximum APD of patient 5 is close to 380 ms. Furthermore, the maximum slope of the restitution curve was also different from patient to patient, ranging from 0.57 for patient 3 to 1.15 for patient 2. Both models (blue and red lines) are shown to reproduce the gray symbols well and overlap for most of the DI range, demonstrating that the model parameters can be adjusted to reproduce a range of restitution curves. One noticeable difference between the two models is that for our fitted parameter sets the KKT model tends to have a larger slope than the FK model for DI less than 50ms. As for the AP morphology, we can quantify the percent error of the model fits (Fig 2.3). We found that for the KKT model the average error over the entire APD restitution curve was less than 1.5% for all patients. For the FK model, the average error was below 1% for all patients. Thus, there was little difference in the error between the FK and KKT models.

2.4.5 CV Restitution Curves

The polynomial fits to the clinical CV restitution data are shown in Fig 2.6 as gray symbols. For three patients (2, 4, and 5) we found that this restitution curve is approximately flat while for patients 1 and 3 it decreases as the DI decreases. This is consistent with earlier reports that found that CV restitution can be flat or can decrease for decreasing DI [LSG$^+$12]. The fits from both

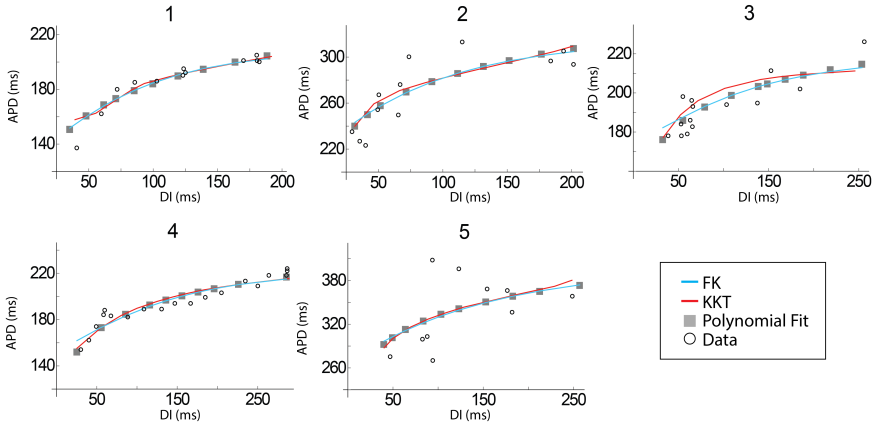

Figure 2.5: Model APD curves can be fitted to clinical data. The clinically determined APD and its polynomial fit are shown as open and closed symbols, respectively, for the 5 patients. The results from the fitting procedure is shown in blue (FK) and red (KKT).

models are shown as solid lines and can be seen to match the clinical data over the entire range of DIs. The average error for the KKT model was found to be less than 1.3% for all patients (Fig 2.3) while the largest single point error is for small DI in the patients with flat CV restitution where the fitted CV differs from the clinical CV by 5.3% (patient 5). The cumulative error in the FK model was less than 1.5% for all patients and the largest deviation from clinical CV is for small DI in patient 3 (6.9%).

2.4.6 Spiral Wave Propagation

Two-dimensional spiral waves were generated for each of the fitted parameter sets in both models. Snapshots of the resulting activation pattern for each patient, including the alternate parameter set for patient 1, are shown in Fig 2.7 where the membrane voltage in the KKT model is shown in a color scale and in the FK model in a gray scale with white (black) corresponding to high (low) voltage.

Both models produced stable spiral waves in 4 out of 5 patients, with patient 2 exhibiting spiral wave breakup. In the lower row of Fig 2.7 we have plotted the trajectory of the spiral tips of the stable spirals (red for the KKT model and blue for the FK model). The trajectories in the

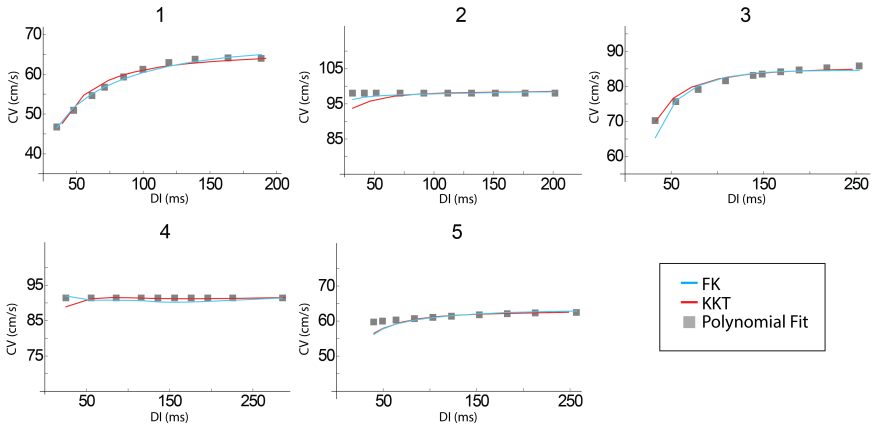

Figure 2.6: The conduction velocity as a function of DI for each of the 5 patients. No raw data was available for the CV restitution curves, though the points calculated from the inverse activation time data can be seen in Fig 2.2. Only the polynomial fit to these is shown here, along with the model curves.

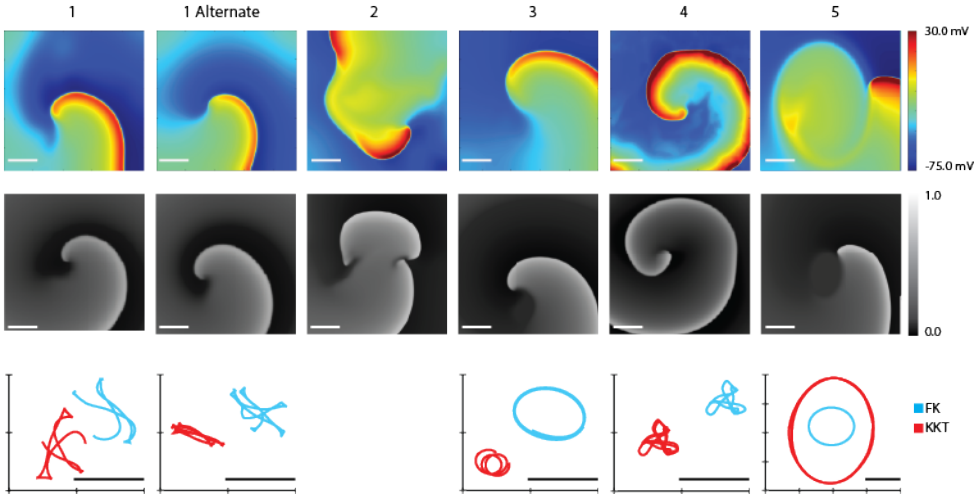

Figure 2.7: Spiral wave patterns in 2D for the fitted parameters sets. The top row shows snapshots of the activation pattern following the initiation of a spiral wave in the KKT model using the fitted parameter set for each patient. The membrane voltage is shown using a color scale. The middle row show snapshots of the activation patterns obtained using the FK model with white (black) corresponding to depolarized (repolarized) tissue. In the bottom row we have plotted the corresponding tip trajectories of the KKT model (red) and FK model (blue). Note that the trajectory location is arbitrary, and that some spirals were spatially translated to facilitate comparison between the models. Scalebar: 2 cm.

two models show a similar pattern for all patients, including the alternative set. The scale of the meander pattern is very similar for patient 1 and 4 while slightly different for patients 3 and 5. The rotation period in the KKT model ranged from 125 ms (patient 4) to 457 ms (patient 5). Spiral wave periods in the FK model were roughly similar, differing from 2% (patient 2; 196 ms for the KKT model and 200 ms for the FK model) to approximately 20% (patient 5; 457 ms vs. 370 ms).

2.5 Discussion

The present study performed detailed analyses of the ability of 2 computational models for atrial tissue, the detailed KKT model and the simpler FK model, to recapitulate APD and CV dynamics and AP morphology in a series of carefully studied patients with clinical AF. We found that the parameters of both the simplified and detailed models can be adjusted to reproduce clinically observed tissue behavior. We also found that these parameters varied significantly from patient to patient and from published parameter sets, indicating the need for personalized model building. Furthermore, we simulated the spiral wave reentry using the model equations parameterized by our fits. The spiral wave dynamics are qualitatively similar for each patient between models. The fact that simplified models produce results that can accurately fit clinical data, can generate similar spatio-temporal dynamics that is similar to the dynamics from detailed models, and have a small computational cost suggests that they might be better suited to model cardiac arrhythmias in spatially extended domains than computationally expensive detailed models.

The current study is in several ways distinct from previous studies which attempted to fit computational models to data [SVNL05, BKO$^+$12, KOC11, CCY$^+$12, DL04]. First, we used clinical data instead of animal or numerical data to modify the parameters of two computational models. Detailed AP and CV restitution data were obtained from the left atrium of 5 patients

with clinical AF at electrophysiological study. Second, our fitting procedure was designed to fit not only temporal dynamics using single cell characteristics but also conduction velocity data, a measure of spatio-temporal dynamics. This was achieved by fitting simultaneously the AP morphology as well as APD and CV restitution curves and adjusting model parameters so as to minimize the difference between clinically determined and numerically obtained tissue characteristics. These tissue characteristics are widely considered to be essential features of cardiac tissue and were obtained using recording electrodes, thus representing measurements at discrete locations within the atrium. Thus, and in contrast to fitting schemes that attempt to fit in a sequential fashion, our final parameter set produces a morphology and restitution curves that are optimal fits to the entire clinical data set.

Our results indicate that we are able to fit the clinical data equally well with the FK model and the KKT model. Both models produce fits that vary less than 7% for the AP morphology and approximately 1% for the APD and CV restitution curves. In our fitting algorithm we allowed parameter values to be increased or decreased by an order of magnitude in the KKT model and allowed a variable range in the FK model. These ranges can clearly be easily adjusted, for example using experimentally obtained restrictions of permissible values. We find that at least several parameters vary significantly (¿ 2-fold) from patient to patient and that every parameter varies significantly in at least one patient (S2-S3 Tables). In addition, we found that there exist multiple parameter sets that fit the clinical data equally well. This was determined by re-computing the best fit using different initial parameter values for patient 1 (S2-S3 Tables). The errors from the two different parameter set are roughly equivalent (Fig 2.3) indicating that both sets have an equal goodness of fit. In the FK model we allowed nearly all parameters (21) to vary while in the KKT model 21 parameters were fitted with many more held constant (S1 Table). These constant parameters were chosen based on their minimal effect on the AP morphology or because they are well-established (for example, the cell size and volume). Not restricting the available parameter space by fixing these values will render the fitting procedure computationally unfeasible. It

should be noted, however, that modifying which parameters can be varied is straightforward. Furthermore, we have explicitly verified that the inclusion of 11 more parameters did not result in an improvement in the fit (see S4 Table).

Our results demonstrate that there can be multiple parameter sets with equal goodness of fit. This is perhaps not surprising given the large dimensionality of the parameter space which can lead to multiple local minima [CCY$^+$12, DL04]. Even reducing this dimensionality, however, does not necessarily guarantee a unique set of parameters that fit a specific data set. For example, we have explicitly verified that reducing the number of fit parameters in the KKT model to 5 (gKs, gK1, gNab, gCab and PNa) can still lead to multiple parameter sets that fit the AP morphology and APD restitution within less than 1% error. For this, we created four trial parameter sets by randomly varying the parameters within 50% of their original values. On average, each of the new, and distinct, parameter sets found by our fitting algorithm varied by 17.0%, 10.0%, 8.7%, and 13.6% from the original values (S5 Table). Thus, even a reduced number of parameters can have multiple local minima in the goodness of fitness space. Of course, these sets produced identical AP morphology and APD restitution, but other model properties, including 2D or 3D activation dynamics, might differ. It is perhaps also not surprising that the parameter sets determined for the detailed KKT model differ from the published ones. The model parameters appear in the explicit descriptions of ion channels which take the form of coupled differential equations. However the structure of these equations and their parameters are derived not only from human ion channel or whole cell data but also from animal cells [NFNS09], that may limit their general applicability to human modeling. In addition, the parameters are not always precisely determined, not all channels might be incorporated into the model, and some data is obtained at unphysiological temperatures. Indeed, several recent detailed comparative studies of detailed models has shown that they can exhibit dynamical behavior that is not consistent with cardiac tissue [WHM$^+$12, CF07, BOCF08]. The fact that our current study produced parameter sets that widely varied from patient to patient points to the need of algorithms that can adjust parameters based on clinical data. This is important,

as human atrial tissue is not homogeneous and different atrial cell types display different AP morphologies [GBR$^+$72]. In addition, pathophysiological remodeling of atrial tissue is likely to be a heterogeneous process [OBK$^+$09a] and requires reformulating the channel parameters [HVND14]. Thus, it is unlikely that a single set of parameters or perhaps even a single model is able to capture the behavior of the entire atrium, and the parameters will need to be adjusted.

We used the results from our fits to simulate spiral wave dynamics in both the FK and KKT model. This is highly relevant for AF since recent mapping studies have revealed that spiral wave reentry plays a central role in AF [NKR12, HHD$^+$14] and that the position of these spiral waves are a promising target for localized ablation [NKS$^+$12]. To better understand and address the role of reentry in cardiac tissue and the best way to ablate, simulations of ionic models in spatially extended domains with the characteristics of a particular patient are thus desirable. To facilitate this comparison we ensured that the upstroke of the AP was similar in both models. With a similar AP morphology and restitution curves, the two models produced spiral wave with very similar dynamics, including stability of the spiral wave, tip trajectory and the spiral wave period. The slight differences between the two models are likely due to electrotonic effects and memory effects [FEH99] that act at timescales that are longer than single stimuli [KDT$^+$04]. The comparison between the two models suggests that simplified models might be more advantageous to use in simulations of spatially extended phenomena than detailed models. Clearly, simulating detailed models is computationally expensive, as it requires solving a large set of stiff differential equations and to date, only a limited number of computational studies have been carried out using detailed models in 2 [SCBF$^+$13] and 3D [CE08, VRT$^+$09, GXS$^+$07]. The FK model, and similar simple models, on the other hand, are computationally much more efficient than detailed models [BOCF08, BCG$^+$], and have been extensively used to model cardiac dynamics of single cells and in 2D [CF11] and 3D geometries [CENF07, FCKR05]. This comes, of course, at the expense of detailed knowledge about the precise role of the channels in normal and abnormal cardiac rhythms. Nevertheless, as we have shown here, the parameters of simplified models can be adjusted to

represent clinical data with equal precision compared to detailed models. Thus, detailed models might not represent cardiac tissue dynamics more precisely than simplified models, making the latter attractive choices for simulations of phenomena that do not depend on specific ion channels or if computational speed is critical. Our fitting procedure is not limited to the data sets we used here and other clinically relevant data can be incorporated. For example, it is possible to include data about the onset of alternans, implicated in the initiation of AF [NFC$^+$11, WNGQ11], without altering the fitting scheme. On the other hand, data that is inherently spatially extensive, for example spiral wave rotation periods, would require simulating activation fronts in 2D. If combined with AP morphology and restitution curve data, it should be possible to use that data to fit model parameters in a simultaneous fashion. Of note, that type of data requires high resolution mapping of activation fronts and is currently unavailable in humans. In addition, modifications in our fitting procedure in which, for example, the AP morphology counts more than the restitution curves are straightforward to implement. It should also be clear that our methodology can be applied to other cardiac tissue, including the right atrium and the ventricles. Furthermore, it can be used to fit data obtained in different parts of the atrium, thus generating model parameters that are adjusted in a regional fashion. The electrophysiological models that are then created can be combined with detailed information about the atrial geometry to create truly patient-specific atrial models [GVR$^+$14, GSK$^+$13, MVB$^+$13]. This might be particularly interesting when applied to diseased tissue [OBK$^+$09a] and could be combined with detailed mapping of structural tissue remodeling to create patient-specific models. These computational models might become an important tool in the study of cardiac arrhythmias, possibly resulting in a deeper mechanistic understanding of AF and the development of novel therapies.

Our study has several limitations. First, CV was estimated from the activation times of electrodes on the same spline. A more accurate determination would require constructing high-resolution isochrones in patient-specific geometries. Also, the AP shape was derived from MAP recordings, which are intrinsically noisy. Furthermore, these MAP recordings only represent

local tissue characteristics and quantifying atrial heterogeneity would require multiple recording sites. In addition, since our MAP electrode was close to the stimulus location, we do not have accurate data for the upstroke part of the AP. Also, our spatially extended simulations are in homogeneous 2D sheets, thus ignoring tissue anisotropy and potential 3D effects. Finally, a quantitative comparison between our spatio-temporal simulations and clinical data is currently challenging and would require accurate patient-specific data on the dynamics of wave fronts. Such a comparison necessitates extending our simulations to include anisotropy and 3D properties and would require detailed data on tissue conduction and atrial geometry, along with highly-optimized fitting algorithms and is the subject of future research.

2.6 Acknowledgments

This work was supported by National Institutes of Health Grants R01 HL122384 (WJR), NSF 1413037 (FF), R01 HL83359 and K24 HL103800 (SMN).

Chapter 2, in full, with minor changes to formatting, is a reprint of the material as it appears in PLoS Computational Biology, 2016. Lombardo, Daniel; Fenton, Flavio; Narayan, Sanjiv; Rappel, Wouter-Jan. The dissertation/thesis author was the primary investigator and author of this paper.

Chapter 3

Systematic Reduction of a Detailed Atrial Myocyte Model

3.1 Abstract

Cardiac arrhythmias are a major health concern and often involve poorly understood mechanisms. Mathematical modeling is able to provide insights into these mechanisms which might result in better treatment options. A key element of this modeling is a description of the electrophysiological properties of cardiac cells. A number of electrophysiological models have been developed, ranging from highly detailed and complex models, containing numerous parameters and variables, to simplified models in which variables and parameters no longer directly correspond to electrophysiological quantities. In this study we present a systematic reduction of the complexity of the detailed model of Koivumaki *et al.* using the recently developed manifold boundary approximation method. We reduce the original model, containing 42 variables and 37 parameters, to a model with only 11 variables and 5 parameters and show that this reduced model can accurately reproduce the action potential shape and restitution curve of the original model. The reduced model contains only five currents and all variables and parameters can be

directly linked to electrophysiological quantities. Due to its reduction in complexity, simulation times of our model are decreased more than three-fold. Furthermore, fitting the reduced model to clinical data is much more efficient, a potentially important step towards patient-specific modeling.

3.2 Introduction

Atrial fibrillation (AF) is the most common cardiac arrhythmia and affects 2-3% of the population in Europe and North America [ZBLC$^+$14]. During AF, the electrical conduction of the heart becomes irregular, resulting in rapid and less efficient beating. AF is difficult to eliminate [CHN$^+$13, Jal11], and the underlying mechanisms remain poorly understood. This incomplete understanding is mainly due to the difficulty of obtaining clinical data that quantify the spatio-temporal dynamics during AF. Based on animal data [GEKS92, GPJ98] and on recent recordings of human AF using basket electrodes [NKS$^+$12, NKR12, NKER12] and high density body surface electrodes [HHD$^+$14] it is believed, however, that spiral waves play a crucial role in the maintenance of human AF. Understanding how these spiral waves form and how they are responsible for the various clinical signatures of AF can potentially result in better treatment options for this serious disease.

Mathematical models can play an important role in improving treatment for cardiac diseases, including AF [Kar13]. Simulations of single cells, tissue sheets, or the entire heart can provide useful insights into the role of different cell or tissue properties in cardiac arrhythmias [CBBH01, QXGW00, Rap01, VJH$^+$02]. A crucial component in these studies is the electrophysiological model that describes the voltage dynamics of a cardiac myocyte. This model consists of a set of coupled differential equations that characterize the ion channels within the cell and the resulting currents. A variety of models exist to characterize the excitation of a myocyte, known as an action potential (AP). These models vary in detail and overall structure and can, along with the ionic channels, also include ionic concentrations inside the cell.

Recent studies aim to improve upon the accuracy and capabilities of previous models [GPV$^+$11, CRN98, MGTG08], such as adding a component to characterize the role of the sarcoplasmic reticulum. This results in increasing detail and complexity as the models add new equations and parameters to further describe electrophysiological properties of the cell. There

are, however, several drawbacks of this added complexity. Obviously, adding equations and parameters comes at the expense of increased computational costs. Furthermore, whether this added complexity leads to improved accuracy is questionable since many channel properties are not well characterized or only measured using animal models. In addition, there is a large cell-to-cell variability within the heart and between different hearts, necessitating different and variable parameter sets. Thus, to develop patient specific modeling, a goal of many current modeling studies [Tra14, MVB$^+$12], would require extensive fitting to patient data. This fitting, however, is generally more difficult to accomplish in detailed models [TMS10]. In a recent study, for example, we were able to fit a detailed cardiac model, the Koivumaki Korhonen Tavi (KKT) model [KKT11], to several clinical data sets but at a large computational cost [LFNR16].

As an alternative to these detailed models, simplified descriptions of cardiac cells have been developed [FK98, KKB$^+$91, NFF$^+$98]. These models are computationally efficient, more intuitive to interpret, and their parameters can be adjusted to reproduce a large variety of spatio-temporal dynamics [FCHE02]. These models, however, characterize only a few key components that do not explicitly represent ion channels. Therefore, their parameters cannot directly be compared to physiologically relevant quantities such as ion channels.

It would therefore be useful to have a model that is simple, needing only a handful of differential equations, while still maintaining parameters that are related to physiological quantities. With this goal in mind, we carry out a reduction study of a detailed cardiac model using the Manifold Boundary Approximation Method (MBAM) [TQ14]. This method is particularly well-suited to reduce the number of parameters in so-called "sloppy" models: models in which many parameters are loosely constrained and which only depend a few "stiff" parameter combinations [BS03a]. It turns out that many systems biology models exhibit sloppiness, which is also characterized by parameter sensitivity eigenvalues that are evenly distributed over many decades [GWC$^+$07]. MBAM uses a geometric and information theoretic approach that can systematically reduce a model in a stepwise fashion [TQ14].

We will focus here on the highly complex and detailed KKT model [KKT11] and carry out a stepwise reduction of parameters and variables using MBAM. We report results on 5 reduced models: 4 corresponding to intermediate reduction steps and one representing the final reduction. We show that these models are able to reproduce the AP shape, and AP restitution curve, linking the AP duration and the stimulus period, of the original model. The final reduction model has significantly fewer parameters and variables than the original one and has a significantly shorter computational time. Thus, its complexity is vastly reduced and approaches that of simplified models, without sacrificing the physiological connection between model parameters and variables and cell properties.

3.3 Methods

As our electrophysiological model, we will use the KKT model of human atrial myocytes [KKT11]. The KKT model was designed to characterize a wide range of quantities, including intracellular concentrations and calcium release from the sarcoplasmic reticulum. Several versions of the model are also presented in the original paper, with variations in complexity and results. Here, we use the vNassIk version of the model, with some modification [KSMT14]. In this version, a subsarcolemmal sodium concentration is added to the cell, along with a hyperpolarization activated potassium current. The model is comprised of 42 differential equations, with over one hundred possible parameters.

In terms of measured quantities, we only look at the action potential produced by the model, not the individual currents or concentrations. Simulations were run using an S1-S2 protocol, with the S1 stimulus always having a 500ms cycle length. These three stimuli were chosen to capture the general shape of the APD restitution curve and to characterize tissue dynamics for both large and small cycle lengths. The action potential shapes generated from the three different S2 stimuli were recorded. This protocol is different from what is described in the

original paper, which used several different pacing protocol, some running for several minutes, to quantify a variety of characteristics in the action potential shape and duration. These long simulation time scales would not be practical with the MBAM method, which requires many repeated simulations per reduction step.

Of the many parameters in the model, the time constants and the parameters that represented the extracellular concentrations, and physical dimensions of the cell were kept fixed. The remaining parameters, containing all the model conductances, diffusion constants, buffer concentrations, and reaction rates, were allowed to vary in MBAM. For the version of KKT chosen here, this equates to a model with 42 variables and 37 parameters. Before beginning the reduction algorithm, all the parameters were first log transformed, $\bar{u} = log(u)$, so that each parameter in the model reduction algorithm can vary between $\pm\infty$. This improves the accuracy of the algorithm, as it increases the range of variability for each parameter and makes them dimensionless quantities.

The MBAM reduction algorithm, further detailed in the Supporting Material, begins by creating a metric tensor of the parameter space manifold [TQ14]. This is done by looking at a set of measured quantities produced by the model (see below), and examining how sensitive these are to changes in the parameter space. More precisely, the metric tensor is the Fisher Information Matrix. The eigenvalues of the metric then give a hierarchy of widths that characterize the parameter space. By moving along parameter space towards the nearest boundary, or shortest width, the dimensionality of the parameter space can be reduced. Furthermore, in order to ensure minimal change in the results, the model advances towards the boundary along the geodesic lines of the manifold.

Sixty time points, twenty from each of the three S2 stimuli, were chosen in total for the data points, or measured quantities, in the reduction algorithm. These points were not evenly spaced along the voltage trace, but rather chosen to include values from the upstroke, repolarization, and resting state of the model (see Figure S1). At the end of each run of the reduction algorithm

the model was evaluated at the limit. This corresponds to setting the parameter(s) that will be removed to either 0, resulting in the elimination of a variable or a term in one of the equation, or ∞, which resulted in a fraction that vanishes. After the reduction step, the new and reduced model was refit to the output of the original model at the same sixty time points mentioned above using a simulated annealing method as described in our earlier work [LFNR16]. The reduced model, along with its new parameters, was then used as input to the MBAM algorithm. This process was repeated until the reduced model could no longer be fit to the original model without significant error, defined as $> 10\%$ in the AP shape (see below).

All matrix manipulation required by the MBAM method was run on a Tesla K40 GPU using the CUDA parallel computing framework. Model simulations were run in serial on a quad-core Xeon E5-2637 CPU. A forward Euler scheme with a time step of 0.01ms was used for the model simulations, and a variable time step was used for integrating the geodesic equation. Each successive step of the algorithm took less time to complete, as the model was reduced in complexity.

Accuracy of the fit was defined through an error function E which measures the discrepancy of the numerical results and the original KKT data as reported earlier [LFNR16]:

$$E = \frac{1}{M}\sum_{i=1}^{M}\frac{|x_i^{sim} - x_i^{KKT}|}{|x_i^{KKT}|}. \tag{3.1}$$

where x_i^{sim} and x_i^{KKT} are the values of the simulation of the reduced and original model, respectively, and where M is the total points that are used in the error function.

3.4 Results

We first determined the parameter sensitivity spectrum of the KKT model. To this end, we first computed the cost function, C, for the change in voltage, V, when parameters deviate

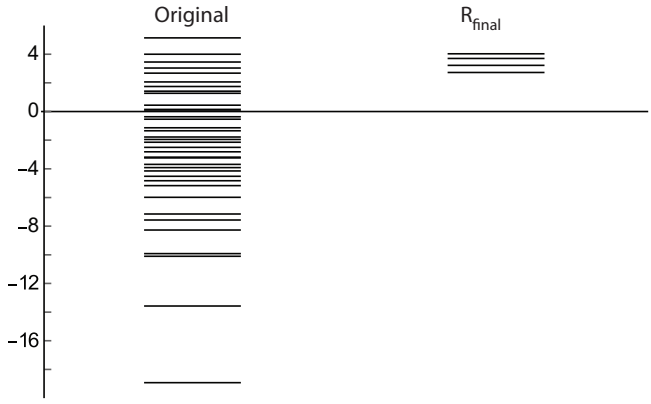

Figure 3.1: Eigenvalue spectrum of the Hessian matrix for the original model and the final reduced model.

from their original values. We use $M = 60$ time points t_m:

$$C = \sum_{m=1}^{M} \frac{1}{2}(V(\vec{\theta}, t_m) - V(\vec{\theta}^*, t_m))^2. \tag{3.2}$$

Here, $\vec{\theta}$ is a vector representing the set of all parameters. We then computed the eigenvalues of the Hessian matrix [GWC$^+$07]

$$H_{i,j} = \partial_i \partial_j C. \tag{3.3}$$

Details of this calculation can be found in the Supplementary Material. The spectrum is plotted in Figure 3.1) and spans roughly 20 orders of magnitude, with eigenvalues that are approximately equally spaced. The latter means that it is not possible to divide parameters into an important and a not so important group.

We next carried out a stepwise reduction of the KKT model with MBAM, and were able to reduce it from 42 variables with 37 parameters to only 11 variables with 5 parameters. In Figure 3.2 we give a visual representation of four intermediate steps along with the final step, showing which parameters are removed after each reduction step. Henceforth we will refer to these steps as R_1, R_2, R_3, R_4, and R_{final}. A similar figure of the change in variables is in Figure S2, and a list of the parameter values for each reduction step is in Table S1.

In this representation, we have marked all parameters that were eliminated in red while the parameters in blue were combined into new parameters. As indicated in Figure 3.2, the red parameters were eliminated in one of two ways. Some parameters, e.g. the conductance of the slow delayed rectifier potassium current, gKs, were set equal to 0, resulting in the complete removal of a current or equation term (Iks in our example). Other parameters appear in the denominator of the current equations and were set equal to ∞. Obviously, this also resulted in the elimination of these terms, together with parameters that appear in the nominator of these equations. These parameter combinations are marked by the bracket and an example is the concentration of the calcium buffer calsequestrin, CSQN, together with its dissociation constant KdCSQN. The parameters marked in blue appear in combinations that can be combined into a single parameter. For example, when going to a boundary of the manifold, both INaKmax, the maximum value of the INaK current, and kNaKNa, the half maximum sodium binding concentration, were observed to grow quickly. Since these parameters are in the nominator and denominator, respectively, they can be combined into a new, and single one ϕ_{INaK}.

The final model contains only 5 parameters, representing the conductances of the 5 remaining currents: the fast sodium current I_{Na}, the L-type Ca2+ current I_{CaL}, the time-independent potassium current I_{K1}, the transient outward potassium current I_t current, and the sustained outward potassium current I_{sus}. These currents are unmodified, except the L-type calcium current which now depends on the parameter ϕ_{CaL}, which is a combination of the conductance and effective reversal potential (see Supplemental Material). The eigenvalue spectrum of the final reduced model R_{final} is shown in Figure 3.1 and shows that the range has significantly decreased from the original model and now only spans 10^4.

We next determined how accurately the reduced models can reproduce the original model results. To this end, we fitted, after each reduction step, the remaining parameters of the model to the data as described in Methods. In Figure 3.3 we plot the computed AP shape for all three S2 stimuli for the 4 intermediate steps and the final reduction step. As can be seen from these graphs,

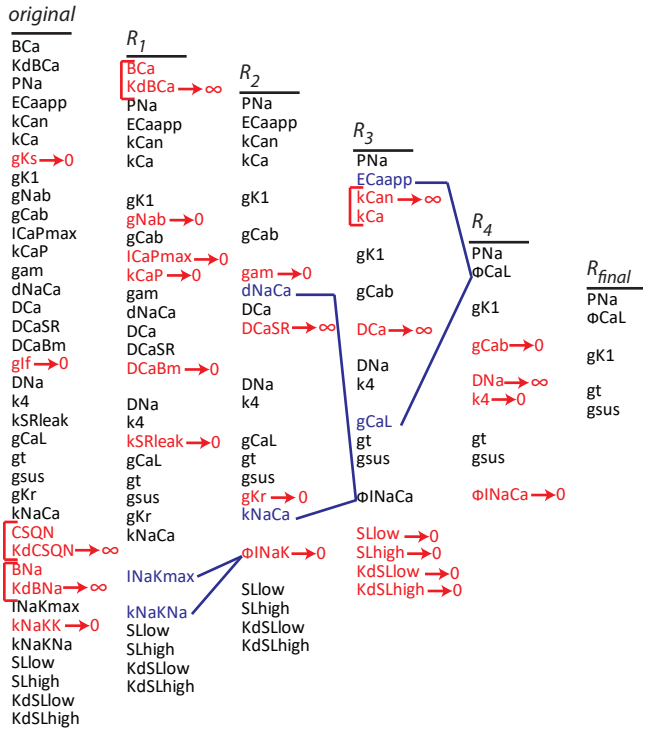

Figure 3.2: Chart of parameter changes between iterations of the reduction algorithm. The parameters highlighted in red are ones that were removed in the following iteration, after being evaluated at a limit. The parameters highlighted in blue were reduced or combined to make new parameters.

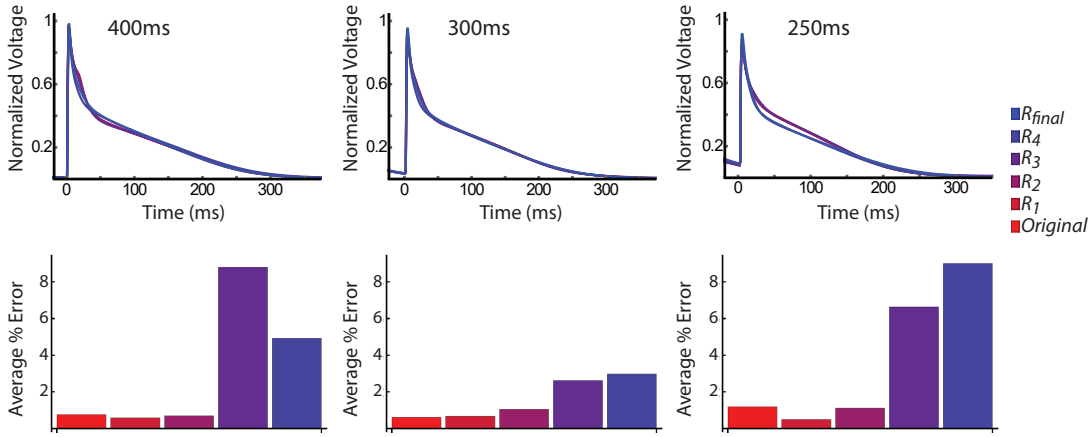

Figure 3.3: AP Shape comparison for select iterations of the reduced model. The AP shape is shown for each of the S2 stimuli in the S1-S2 pacing protocol used in the reduction algorithm.The cycle lengths shown are 400ms, 300ms, and 250ms. For clarity, the bar graph next to each curve shows the percent error in each of the models.

the AP shape remains close to the original one for all reduction steps. This can be quantified by computing the error between the original and the simulated AP curves (see Methods). The results are shown as bar graphs in Figure 3.3 and demonstrate that this error remains $< 2\%$ for R_1, R_2, and R_3 and becomes at most $\approx 8\%$ for R_4 and R_{final}.

To further quantify the outcomes of the reduction steps we computed the APD restitution curve for our three S2 values. The results are plotted in Figure 3.4 using the same color scheme as in Figure 3.2. As expected, the restitution curves for all reduction steps are similar to the one from the original model. In Figure S3 we have plotted APD restitution curves for a larger range of S2 stimuli, showing identical qualitative behavior.

Attempting to proceed after R_{final} resulted in either the conductance of I_{K1} or of I_{sus} to go to 0. Fitting the resulting AP shape with these currents removed resulted in an error that was larger than 10% and the reduction process was stopped. We have also examined the stability of the action potential duration for each of the models, a desirable feature for cardiac simulations [WHM$^+$12]. We found that the original model and the final model are roughly identical in their stability (see Figure S4), while the drift from the initial values was more pronounced in the

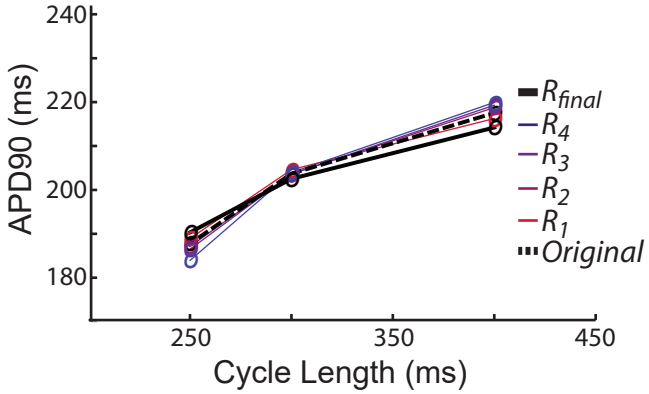

Figure 3.4: APD Restitution curve for the original and reduced models. The APD was recorded from simulations using 3 S2 stimuli, as in the reduction/fitting process. The original and R_{final} models are represented as thick black lines, with the original also being dashed.

intermediate models. The fact that the intermediate models show a more significant drift in voltage is perhaps not surprising. The resting potential is a result of a delicate balance between all currents, pumps and exchangers. Removing some of these might result in a resting potential that slowly changes over time. Furthermore, even the original model shows a small drift. It also likely that constraining parameter values or further fitting with more data points, can improve the stability of the reduced models.

3.5 Discussion

In this study, we systematically reduced a detailed model for atrial myocytes, containing many parameters and variables, to a relatively simple model with only 5 parameters and 11 variables. The reduction was carried out with MBAM, a geometric and information theoretic technique particularly well-suited for sloppy models. This sloppiness is manifested in the insensitivity of the model results to large parameter variations, as shown in the large and roughly even spread of eigenvalues (Figure 3.1). Therefore, the model is only sensitive to a limited set of parameter combinations and should be amenable to parameter reduction.

Many of the currents in the original model were completely removed in the final reduced

version. Perhaps this is not a surprise when one takes into account the result from previous studies. In the original publication of the KKT model [KKT11], it was reported that the addition of the hyperpolarization activated current I_f was added to the model but that it only has a small effect on the overall dynamics, as it only activates at very low voltages. It is also stated that the I_{Ks} and I_{Kr} currents in the model should have a smaller effect than the I_{K1} current in determining repolarization. In agreement with this, our method removes the I_f, I_{Kr}, and I_{Ks} currents entirely, while keeping the I_{K1} current. Furthermore, Nygren *et al.* shows that the I_{CaP}, I_{Nab}, I_{Cab}, I_{NaK} and I_{NaCa} currents are more relevant for maintaining sodium and calcium concentrations within the cell and do not change the response of the cell to a stimulus in a significant way [NFF$^+$98]. As the goal of our reduced model was to characterize the action potential, it is reasonable that currents related to the ionic concentrations could be removed. Clearly, since our final reduced model does not explicitly solve for these concentrations, nor for the calcium concentration within the sarcoplasmic reticulum, it will not be able to address dynamics changes of these concentrations. We should point out, however, that some of these variables are still present in one of the intermediate models, which could be used instead. Furthermore, our reduction method focused on the voltage dynamics, using an S1S2 stimulus protocol. Reduction attempts that focus on the dynamics of some of the intracellular components might result in reduced models that maintain the ability to investigate the ionic concentrations.

Our final model resulted in AP changes and restitution curves that are close to the ones generated by the original model even though it contains many fewer variables and parameters. This suggests that our reduced model can be used as a viable alternative to the complex full model for the investigation of the response of both single to different stimuli and for the study of spatio-temporal dynamics in spatially extended geometries.

When trying to further reduce the model by eliminating one of the remaining 5 currents, the error in the resulting and the original AP shape became quite large. This suggests that using the ionic formulation of the KKT model it is not possible to accurately describe AP shapes without

an explicit description of I_{Na}, I_{CaL}, I_{K1}, I_t, and I_{sus} and that our reduced model can be seen as a minimal atrial myocyte model. This does not mean that it is impossible to fit AP shapes with fewer variables, as, for example, in the Fenton-Karma model [FK98]. This model, however, does not utilize the same functional form for its variable equations which can no longer be directly equated to ionic currents.

While many of the components of the original KKT model were removed, this approach has also allowed for much of the detail and complexity to remain in the five currents that were kept in the model. Of these currents, only the L-type calcium channel was altered, and a physical description can still be associated with many of the parameters and variables. This is in contrast to the simple models that have been developed in the past. Not surprisingly, our reduced model is computationally more efficient than the original one. An estimate of the simulation times for the original and for the final model shows that the reduction resulted in an approximately three-fold speed-up: simulations of 1000s for a single cell took 11.9, 11.1, 9.7, 8.6, 6.6, and 3.7 seconds for the original, R_1, R_2, R_3, R_4, and R_{final} models respectively. We have verified that similar a speed up can be seen when fitting the model to data, a task that is necessary for the development of patient-specific models.

3.6 Conclusion

Here, we showed how MBAM can systematically reduce the complexity of a detailed atrial model. Although we have focused here on a model for atrial myocytes, our reduction methodology can also be applied to models for ventricular myocytes [tTP06]. The models presented here are capable of reproducing action potential dynamics that are equivalent, or nearly equivalent, to those produced by more detailed models. The approach used in this paper begins with a very complex model and successively removes all components which did not greatly affect the action potential or the APD. Meaning that only variables and parameters which have the

greatest sensitivity to the measured quantities remain. Plus, this produces a series of increasingly simple models, instead of a single end result. From the final reduced model, we find that I_{K1}, I_{sus}, I_t, I_{Na}, and I_{CaL} currents are most relevant for determining AP shape and duration. We conclude here that if one does need to study all the intricacies of intracellular concentrations, then a detailed model containing such components is not necessary for studying many of the remaining dynamics.

3.7 Acknowledgments

This work was supported by National Institutes of Health R01 HL122384.

Chapter 3, in full, with minor changes to formatting, is a reprint of the material as it appears in Chaos, 2017. Lombardo, Daniel; Rappel, Wouter-Jan. The dissertation/thesis author was the primary investigator and author of this paper.

Chapter 4

Chaotic tip trajectories of a single spiral wave in the presence of heterogeneities

4.1 Abstract

Spiral waves have been observed in a variety of physical, chemical, and biological systems. They play a major role in cardiac arrhythmias, including fibrillation where the observed irregular activation patterns are generally thought to arise from the continuous breakup of multiple unstable spiral waves. Using spatially extended simulations of different electrophysiological models of cardiac tissue, we show that a single spiral wave in the presence of heterogeneities can display chaotic tip trajectories, consistent with fibrillation. We also show that the simulated spiral tip dynamics, including chaotic trajectories, can be captured by a simple particle model which only describes the dynamics of the spiral tip. This novel result shows that spiral wave breakup, or interactions with other waves, are not necessary to initiate chaos in spiral waves.

4.2 Introduction

Spiral waves are generic dynamical states of spatially extended excitable systems. They are observed in a variety of biological and non-biological systems, including aggregates of Dictyostelium discoideum cells [LCG96], chicken retinas [GB83], surface catalytic oxidation reaction systems [JRE+90], and in chemical Belousov-Zhabotinsky systems [ES96, Win72]. Spiral waves can also form in cardiac tissue, where they are believed to play a critical role in life-threatening arrhythmias [Kar13]. In particular, they are responsible for the maintenance of fibrillation during which the activation pattern of the tissue is incoherent, resulting in insufficient pumping of blood [GEKS92, GPJ98, NKS+12, NKR12, NKER12].

Spiral waves are characterized by a tip, corresponding to a phase singularity, and a rotating wave that propagates outwards. Simulations have revealed that the tip trajectory of a single, stable spiral wave can trace a variety of periodic patterns [Win91, ZH95, QWG00, QXGW00]. Many computational studies have also demonstrated that spiral waves can be unstable, even in homogeneous domains [Kar13, FCHE02, ZKB17, FNC+11]. This instability leads to continuous breakup and formation of new spiral waves, accompanied by removal of spiral waves through collisions. This multi-wave state results in incoherent activity, consistent with recordings of fibrillation.

Recent studies in humans have demonstrated the existence of spatially localized spiral sources during atrial fibrillation [NKS+12, NKR12, NKER12, HSC+16]. The removal of these sources can result in acute termination of fibrillation, suggesting that these localized spirals are the driving factor of fibrillation. In this case, fibrillation would not require a multi-spiral state but, instead, can be due to a single spiral wave. Consistent with this hypothesis is that tracking of the spiral tip of the localized source has revealed that it does not appear to trace a regular path, but instead displays a complex trajectory [NKR12, HHD+14]. Thus the question arises: Can a single spiral exhibit irregular tip trajectories, and can it generate irregular activations patterns even in

the absence of spiral wave breakup?

We address this question by computationally examining the trajectory of a single spiral wave in the presence of tissue heterogeneities, modeled as small regions with decreased excitability. The inclusion of heterogeneities is motivated by the observation that cardiac tissue is rarely homogeneous and typically exhibits variations either due to inherent differences in cell properties [Ant07] or due to injury and disease such as ischemic fibrosis [OBK$^+$09b]. Previous numerical studies have shown that a spiral wave can be attracted to an isolated heterogeneity, causing it to eventually be anchored and resulting in a regular activation pattern [ZLK93, XQG98, Olm10, ZP12, XQG98, ZKB17, DDP13]. Furthermore, a recent study has shown that multiple heterogeneities can have a profound impact on the stability of spiral waves and can result in chaotic activation patterns consisting of multiple spiral waves [BBPL17]. Here, we will show that the tip trajectory of a single spiral can become chaotic in the presence of just two small heterogeneities and that these dynamics can be captured by a simple model in which the tip is represented by a particle in a force field.

4.3 Electrophysiological Models

We start with a standard model for cardiac tissue which describes the potential u of cardiac cells as

$$\frac{du}{dt} = D\nabla^2 u - \frac{I_{ion}}{C_m}. \tag{4.1}$$

Here D is a diffusion coefficient responsible for the spreading of the activation front and C_m is the capacitance of the membrane. I_{ion} represents the membrane currents and models for these currents range from relatively simple to very detailed [ABE16]. To stress the generality of our results, we used both a simplified electrophysiological model, the Fenton-Karma (FK) model [FK98] which contains only 3 currents and 13 parameters, and the detailed Koivumäki, Korhonen,

and Tavi (KKT) model, which contains 13 currents and more than 40 parameters [KKT11]. The parameters of the FK model can easily be changed to fit different electrophysiological data, including human [FCHE02, LFNR16] while the KKT model has been specifically developed for human atrial tissue [KSMT14, WHM$^+$12, LR17]. Details of these models and the numerical implementation can be found in the Supplemental Material.

We first focused on the FK model, which can produce a variety of stable, regular single spiral trajectories in homogeneous media by varying just a few of the parameters [FCHE02]. In Fig. 4.1A and C we show examples of a stable circular and a flower-like trajectory with inward petals. We will call the parameter sets responsible for these trajectories set I and set II, respectively (Table S1). The power spectrum of the time series of the x coordinate of the tip for set I show a single peak while for set II it shows two peaks (Fig. S1). To examine how the model behaves in heterogeneous media, we added two identical, circular regions with decreased excitability to the computational domain. Within these regions we increased the value of the time constant of the fast inward current, thus mimicking a domain with decreased conductance (see Supplemental Material). For consistency, the initial conditions used in each simulation consisted of a spiral wave in the lower left region of the sheet. We adjusted the size and spacing between the heterogeneities, and quantified their effects on the dynamics of the spiral wave trajectory.

Our simulations revealed that the presence of the two circular heterogeneities can dramatically alter the tip trajectory of the spiral wave and the activation patterns of the tissue. This is shown in Fig. 4.1B and D where we have plotted phase diagrams of the tip trajectory found in the simulations corresponding to set I and II. In these diagrams the x-axis represents the heterogeneity size while the y-axis represents the spacing between heterogeneities. Since very small heterogeneities leave the trajectory unaffected, we only focus on heterogeneity sizes that are large enough to alter the tip behavior. Also, note that since the distance between the heterogeneities is at least twice their radius, the phase diagram is only shown above the line $y = 2x$. The phase diagram shows that for small spacings, the spiral wave is anchored to both heterogeneities and

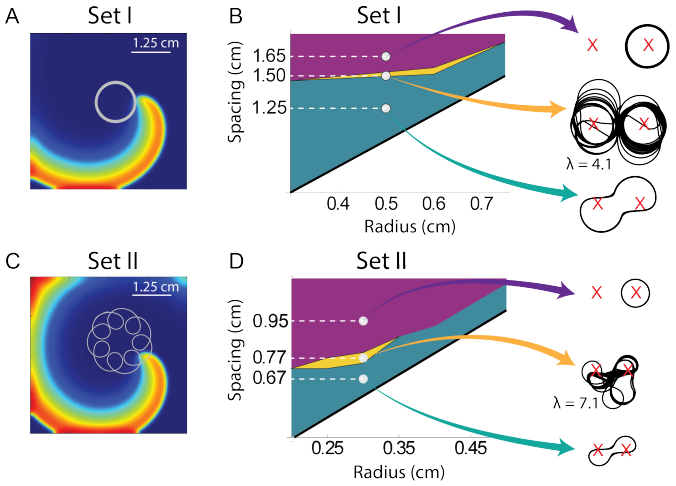

Figure 4.1: A, C: Snapshot of a counter-clockwise rotating spiral wave for two different parameter sets of the FK model (voltage color-coded ranging from high (red) to low (blue) values, tip trajectory shown in white). B, D: Phase diagrams in the spacing-size space for the FK model. Blue area indicates regular trajectories that wrap around both heterogeneities, purple region represents tip trajectories that circle either one of the heterogeneities, and yellow region corresponds to chaotic trajectories. Displayed spiral tip trajectories correspond to the white dots in the phase diagram. Red X's mark the locations of the circular regions with decreased excitability. Lyapunov exponents for the chaotic trajectories are given in units of bits/second.

orbits around them (blue region, Fig. 4.1B and D), while for large spacings the spiral wave rotates around one of the two heterogeneities (purple region, Fig. 4.1B and D). The regular, periodic spiral tip trajectories corresponding to a representative point within these two regions are also shown in Fig. 4.1B and D. Interestingly, there is a region in phase space between these two regular domains for which the trajectory becomes irregular. Within this region, the spiral tip alternately circulates, in a non-periodic fashion, around one or the other heterogeneity. Thus, the presence of a pair of heterogeneities is sufficient to drastically alter the tip dynamics of a single spiral and to render it irregular. To ensure this behavior is not caused by the boundary conditions, we have confirmed that doubling the domain size produces similar results. We further verified that the spiral wave does not breakup into multiple waves, and remains a single spiral throughout the simulation.

To quantify the dynamics of the irregular trajectories, we computed the leading Lyapunov exponent, λ, measures the rate of exponential divergence of nearby trajectories using a standard

procedure [WSSV85] (see also Supplemental Material). We found that λ for the irregular patterns, corresponding to the yellow region in the phase diagrams of Fig. 4.1B and D, was large and positive while for the regular tip trajectories it was close to zero. Therefore, our simulations show that the presence of heterogeneities and a single spiral wave are sufficient to produce chaotic dynamics.

We then investigated the KKT model [KKT11, KSMT14] which, in homogeneous tissue, exhibits a spiral wave that is stable, with a tip trajectory that shows a flower pattern with outward petals (Fig. 4.2A, Table S2). The power spectrum of the tip coordinates again shows only two dominant frequencies (Fig. S1). We then added circular heterogeneities by decreasing the permittivity of the sodium channel I_{Na} to half of its original value. Since this model is computationally much more demanding than the FK model, we did not map out the entire phase space shown in Fig. 4.1. Instead, we fixed the radius of the heterogeneities to 0.5 cm and varied their spacing, corresponding to a cut through phase space. The results are shown in Fig 4.2B where we have plotted the tip trajectory for different spacings of the heterogeneities. As in the case of the FK model, the KKT model shows regular dynamics when the spacing is small, with a tip trajectory that spans both heterogeneities, and when the spacing is large, corresponding to the tip rotating around one of the heterogeneities. For intermediate spacings, the trajectory alternates in a non-regular fashion between the two heterogeneities and computing the Lyapunov exponent revealed that the dynamics was chaotic. Thus, as found in the FK model, a single spiral wave in the presence of heterogeneities can produce chaotic activation patterns.

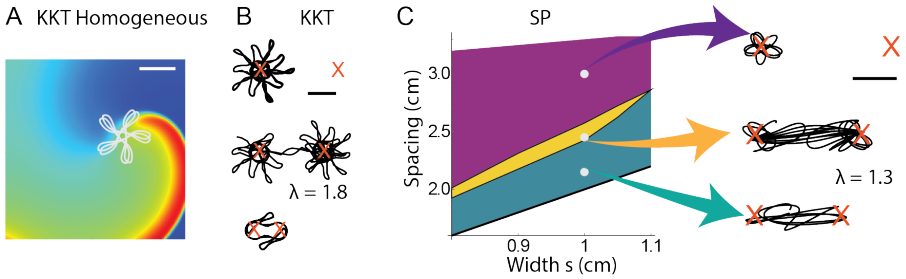

Figure 4.2: A: Snapshot of a counter-clockwise rotating spiral wave in the KKT model. B: Sample tip trajectories of the KKT, for different spacings of heterogeneities with radius 0.5cm. C: Phase diagrams of tip trajectories for the SP model. All scale bars are 1cm. See also Fig. 4.1.

4.4 Single Particle Model

To gain further insights into the surprising transition between regular and chaotic behavior of a single spiral wave, we constructed a simple model in which the tip trajectory is described by a single particle moving in a potential landscape and subject to periodic forcing terms. The idea that the dynamics of spiral tips can be described by particles has been suggested in previous work [BB03, LB13, XLQD12, Bar94]. Here, the aim is to describe the transition between regular and chaotic trajectories shown in our spatially extended simulation. Our single particle (SP) model consists of equations for the x and y coordinates of the tip in the presence of external forces and heterogeneities. To reproduce the tip trajectories in homogeneous tissue we include two forcing terms with frequencies ω_1 and ω_2 and amplitudes F_1 and F_2, respectively. We note that, if necessary, it is trivial to extend the equations to include forcing terms with more frequencies. Our equations take the form:

$$\frac{d^2x(t)}{dt^2} = F_1\cos(\omega_1 t+\phi)+F_2\cos(\omega_2 t)-\xi\frac{dx}{dt}-\frac{dU(x,y)}{dx}. \tag{4.2}$$

$$\frac{d^2y(t)}{dt^2} = F_1\sin(\omega_1 t)+F_2\sin(\omega_2 t)-\xi\frac{dy}{dt}-\frac{dU(x,y)}{dy}. \tag{4.3}$$

where the phase ϕ determines whether the pattern is inward ($\phi = 0$) or outward ($\phi = \pi$) and where the third term represents a damping that prevents the model from drifting and allows it to converge

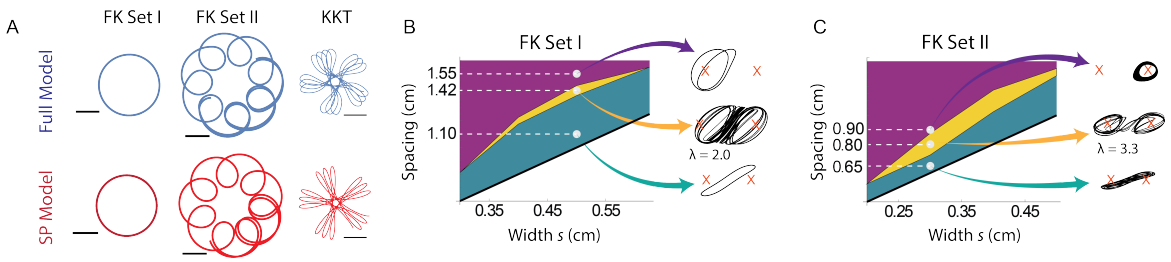

Figure 4.3: A: Comparison between the full models (FK, KKT) and SP model for homogeneous media. Scale bars are 0.5cm. B, C: Phase diagrams of tip trajectories for set I (B) and set II (C) in the SP model, with tip trajectories and Lyapunov exponents. See also Fig. 4.1.

to a steady state quickly. The last term in the model describes a potential energy landscape that can be added to model heterogeneities and which is described below.

For the case of homogeneous media ($U(x,y) = 0$) the model can be trivially solved and the parameters can be immediately determined from the tip trajectory computed using the spatially extended electrophysiological models. First, the frequencies ω_1 and ω_2 are simply the frequencies obtained from the power spectrum of the trajectory (Fig. S1). The value of ω_1 is related to the overall period of the spiral, while ω_2 is the angular frequency of the petals in the flower patterns. Second, the amplitudes of the forcing terms, F_1 and F_2, are determined by the overall size of the trajectory, and the size of the petals (Fig. S1). Explicit expressions that relate these amplitudes to the trajectory dimensions are given in the Supplementary Material, along with the complete solution for the homogeneous case. Obviously, for circular tip patterns $\omega_2 = 0$ and $F_2 = 0$ and the model contains only a single forcing term. As expected, the SP model is able to faithfully reproduce the tip trajectories for the homogeneous cases. This is shown in Fig. 4.3A where we plot the trajectories for the FK and KKT models (blue) along with the trajectories of the corresponding SP model (red). The parameters of these SP models are listed in Table S3.

We next investigated the effect of including heterogeneities in the SP model, keeping the forcing parameters fixed to the values determined for the homogeneous case. Circular heterogeneities can be incorporated in the SP model by introducing a potential energy term of the

form:

$$U(x,y) = -\frac{g}{\sqrt{2\pi}}\left(\exp[-\frac{(x-c_{x1})^2+(y-c_{y1})^2}{2s^2}]+\exp[-\frac{(x-c_{x2})^2+(y-c_{y2})^2}{2s^2}]\right) \quad (4.4)$$

In this potential, the heterogeneities are described by two Gaussian wells with circular symmetry that are centered at coordinates (c_{x1}, c_{y1}) and (c_{x2}, c_{y2}), respectively (Fig. S2). The width of the Gaussian well, s, determines the size of the heterogeneous region. The parameter g controls the depth of the wells, and therefore the strength of the heterogeneities. Very small values of g, similar to minor conductance variations in the electrophysiological models, will not result in significantly changed tip trajectories. Very large values, on the other hand, corresponding to fully non-conducting regions, will result in trajectories that are trapped by the heterogeneities. Here we report results for a value of $g = 0.0022 cm^2/ms^2$ to match the dynamics of Set I and II, and $g = 0.0088 cm^2/ms^2$ for matching the KKT spiral dynamics.

We then determined whether the SP model in the presence of heterogeneities was able to reproduce the FK and KKT results. Fig. 4.3B and C show phase diagrams and tip trajectories for the SP model with parameters based on Set I and II of the FK model. For both sets, the phase diagrams are qualitatively similar to the ones obtained using the FK model (Fig. 4.1B and D). Specifically, for small spacing, the trajectory migrates around both heterogeneities while for large spacing the particle circles around one of the two heterogeneities. In both cases, the trajectory dynamics is regular with a Lyapunov exponent close to zero. For intermediate spacings, however, there is a region in parameter space for which the spiral tip describes an irregular pattern. In this region, the largest Lyapunov exponent was found to be large and positive, indicating chaotic particle trajectories. In Fig. 4.2C we show the phase diagram results for the SP model with parameters corresponding to the KKT model. Note that contrary to the KKT model, it is computationally trivial to obtain this diagram. The phase diagram shows a similar structure as the phase diagram for the FK model with a chaotic region sandwiched between regular and periodic

regions. The trajectories within these regions show good agreement with the ones obtained using the KKT model. We should point out that anisotropy can also be included into the SP model by modifying the forcing terms for the x and y coordinates, as shown in the Supplemental Material and Fig. S3.

4.5 Discussion

Since the SP model only describes the tip and not the entire spiral wave, these results show that the tip dynamics does not critically depend on the properties of the spiral wave arms. Furthermore, our results demonstrate that the existence of a chaotic regime for a single spiral wave in the presence of heterogeneities is not dependent on the specifics of the model, but rather a generic property of spiral waves.

Finally, we show that these results are not limited to a pair of heterogeneities by examining the trajectories of the models in the presence of six, equal sized heterogeneities, randomly assigned to a coarse grid. For some of these configurations, the FK model displays a regular, periodic trajectory, as seen in Fig. 4.4A. Importantly, this trajectory is captured very well by the SP model, again using model parameters corresponding to the homogeneous case (Fig. 4.4B). We have verified that this correspondence holds for 9 out of 10 randomly selected configurations. Furthermore, for some configurations the FK model displays a chaotic trajectory, as determined by computing the Lyapunov exponents (Fig. 4.4C). This chaotic dynamics is also consistent with the dynamics obtained by the SP model for the same configuration, again demonstrating that the simple particle model is able to fully capture the dynamics of the more complex spatially extended model (Fig. 4.4D). To determine the effect of the chaotic spiral tip trajectory on recordings of electrical activity, we computed the electrocardiogram (ECG) at a location near one of the heterogeneities [WIT08]. As seen in the inset of Fig. 4.4C, the ECG is irregular, resembling ECGs seen during cardiac fibrillation. Importantly though, this irregular ECG is not

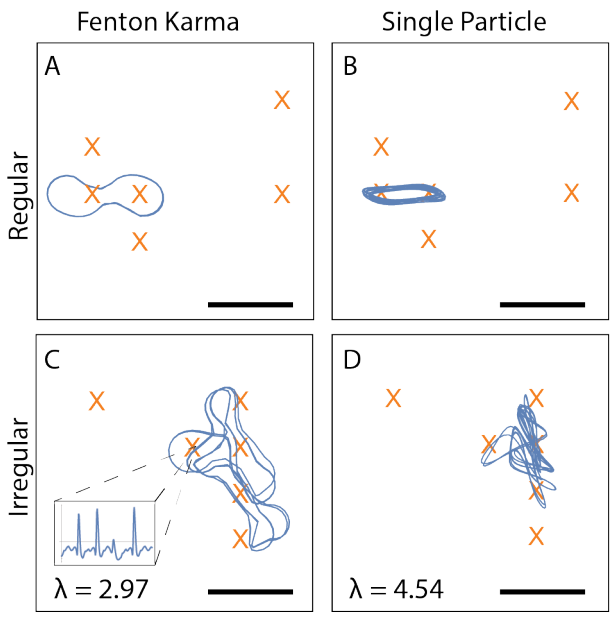

Figure 4.4: Spiral trajectories for the FK and SP models in the presence of six randomly placed heterogeneities. Regular (A, B) and chaotic (C, D) trajectories with matching placement of the heterogeneities. The radius of the heterogeneities in the FK model was 0.3cm, and the *s* parameter in the SP model was 0.275cm. All scale bars are 1cm.

due to spiral wave breakup but is solely due to the presence of a single spiral wave with a chaotic tip trajectory.

To summarize, we have demonstrated that the presence of a pair of heterogeneities is sufficient to change the tip trajectory of a single spiral from periodic to chaotic, demonstrating that spiral wave breakup is not required to generate complex and irregular activity. We have also developed a model of the spiral tip trajectory with parameters that can be directly determined from tip trajectories obtained using spatially extended simulations. This model can accurately capture both the stable spiral tip trajectories observed in spatially extended models and the transition from periodic to chaotic trajectories. Our results indicate that this transition is largely independent of the dynamics of the spiral wave arm and the type of electrophysiological model.

Acknowledgments

We gratefully acknowledge the support of NVIDIA Corporation with the donation of the Tesla K40 GPU used for part of this research. This work was supported by National Institutes of Health R01 HL122384.

Chapter 4, in full, with minor changes to formatting, has been submitted for publication of the material as it may appear in Physical Review Letters, 2018. Lombardo, Daniel; Rappel, Wouter-Jan. The dissertation/thesis author was the primary investigator and author of this paper.

Appendix A

Appendix to Chapter 2

A.1 Detailed Methods

A.1.1 Data acquisition from MAP catheter

The signal was processed by first filtering it between 0.05 to 500 Hz. An average AP curve was constructed by normalizing the AP shapes for all CLs (see Fig. 2.1). Our clinical data contains several AP shapes (between 4-9) for each CL. This can be used to compute a distribution of shapes, along with a standard deviation as a measure of variance between individual shapes. For example, for patient 2, we find that this standard deviation ranges from 1% to 10% while for patient 4 it ranges from 1% to 27%. We can compare this variance to the standard deviation as computed between all normalized AP shapes and the canonical AP shape. This computation yields a variance of roughly 2% to 10%, and 3% to 23% for patient 2 and 4, respectively, indicating that the degree of uncertainty per CL is similar to the degree of uncertainty for all CLs. Thus, it is justified to use a canonical AP shape.

Since the MAP electrode was close to the pacing electrode, the first 30 ms of each AP morphology was discarded and the value of the voltage at 30 ms was assumed to be 50% of the maximum upstroke, based on recording studies of isolated human atrial cells [WMR$^+$12],

while the potential at t=0 was set to the maximum upstroke value. The potential was rescaled to have values between 0 and 1 and was then fitted to a twelfth-order polynomial (see Fig. 2.1). Action potential duration (APD) was determined using validated software [FKFZ95] with manual verification. After assigning AP onset as time of maximal computed upstroke (dV/dt), we determined APD90 as the interval from AP onset to 90% voltage recovery from phase II. Diastolic interval (DI) spans the interval from APD90 of the previous beat to AP onset and for each patient the minimum and maximum DI values (DImin and DImax) were determined. The resulting APD restitution curve, relating DI and APD, was fitted using a logarithmic function of the form $a0 + a1 * ln(DI)$. CV restitution was assessed at multiple atrial sites by analyzing activation times at each of 64 electrodes of a basket electrode. A basket catheter (Constellation, Boston Scientific, Natick, MA) was inserted into the left atrium through a trans-septal sheath by experienced operators, taking care to ensure good contact [NKS$^+$12]. Activation time was then determined at each site using semi-automated software based on the most negative dV/dt from the filtered isoelectric baseline between paced activations. The relative dependence of activation times on the CL, and thus the shape of the restitution curve, was determined by averaging the inverse activation time over all sites for each CL value. The maximum CV was computed from the difference in activation time between the electrode closest to the stimulus site, displaying the earliest activation after simulation, and its neighboring electrode along the same spline, located at a fixed distance of 4 mm. Finally, the CV restitution curve was obtained by using the CL vs. DI data and by fitting a function of the form a0+a1/DI+a2/DI2+a3/DI3 to the data points (see Fig. 2.2). This resulted in CV values for a range of DI (DImin to DImax).

A.1.2 Model Implementation

The KKT model discussed in Chapter 2 extends earlier detailed models [NFF$^+$98, MGTG08] to account for Ca2+ dynamics in the sarcoplasmic reticulum and consists of 43 variables and more than 100 parameters [NFF$^+$98, KKT11]. Attempting to fit all parameters

is computationally challenging and we therefore restricted the number of variable parameters. Specifically, all spatial dimensions, such as the length of the cell, and radius and width of the bulk cytosol, were kept constant. In addition, the membrane capacitance, low and high phospholipid concentrations, phospholipid dissociation constants, and extracellular concentrations were fixed. Also, varying the parameters for the sodium-potassium exchanger current typically caused the model to produce unphysical results including oscillations and these parameters were held constant. Finally, we performed a sensitivity analysis using the parameter values of the original study. In this analysis, we decreased every parameter value in turn by 80% and determined the resulting change in the APD and AP shape of a single computational cell. Parameters that led to a total change that was less than 20% were held constant throughout our fitting procedure. Of the 13 parameters determined in this way, two were found to result in improved fitting results and were included into our group of variable parameters. The final result is a set of 21 parameters that were allowed to vary and which are specified in S1 Table. The initial values of these parameters were chosen to be the ones reported in the original study [KKT11] and parameter values were allowed to change by a factor of 10 in either direction. After completing the fitting procedure with 21 parameters the fitting algorithm was repeated with the inclusion of 11 more parameters (BNa, KdBNa, INaKmax, kNaKK, kNakNa, gt, gsus, gKr, gCaL, gIf), but no improvement was found in the fit. In order to decrease the computation time of the simulations, extensive look-up tables were used for the currents [CBC$^+$11]. To better facilitate comparison of model and clinical AP morphologies, we rescaled the membrane potential so that its maximum value in the entire S1-S2 stimulus sequence corresponds to 1 and its minimum value to 0.

The FK model [FK98] discssed in Chapter 2 replaces the detailed description of the numerous atrial ion channels with a minimal set of equations that can accurately describe key dynamical features of cardiac tissue. The model contains only 3 or 4 variables, together with a limited number of parameters that can be modified to reproduce AP shapes originating from detailed models [FK98, FCHE02] and experiments [CF08]. In this study, we employed a version

of the FK model which consists of four variables, three gating variables and the membrane potential, and 24 parameters [CENF07]. The equations for the gating variables v,w, and d read:

$$\frac{dv}{dt} = \frac{(1-\theta(u-u_n a))(1-v)}{(1-\theta(u-u_v))t_v^- + \theta(u-u_v)t_{v2}^-} - \frac{\theta(u-u_{na})v}{t_v^+}. \tag{A.1}$$

$$\frac{dw}{dt} = \frac{(1-\theta(u-w))(1-w))}{t_w^-} - \frac{\theta(u-u_w)w}{t_w^+} \tag{A.2}$$

$$\frac{dd}{dt} = (\frac{1-\theta(u-u_d)}{t_s^-} + \frac{\theta(u-u_d)}{t_s^+}) * (\frac{1+tanh(x_k(u-u_{csi}))}{2} - d) \tag{A.3}$$

where v and w represent the fast and slow gating variable, respectively. The third gating variable is added to the original version of the model [FK98] to improve the shapes of the AP and CV restitution curves [CENF07]. These gating variables vary between zero and one, with zero being completely closed and one being completely open, and result in a fast inward, slow inward, and slow outward current. These currents, along with the equation for the time constant tso, are given by:

$$I_{fi} = -\frac{v * (u-u_n a) * (u_m - u) * \theta(u-u_n a)}{t_d} \tag{A.4}$$

$$I_{so} = \frac{(u-u_o)(1-(u-u_c))}{t_o} + \frac{\theta(u-u_c)}{t_{so}} \tag{A.5}$$

$$I_{si} = -\frac{w * d}{t_s i} \tag{A.6}$$

$$t_{so} = t_{soa} + \frac{1}{2}(t_{sob} - t_{soa}) * (1 + tanh((u-u_{so})x_{tso})) \tag{A.7}$$

The values of u_o, u_m, and u_{na} were set to 0.0, 1.0, and 0.23 respectively, while the values of the remaining 21 parameters were determined using our fitting procedure. As initial conditions

for these parameters we used set 3 of Ref. [FCHE02], modified to the 4 variable version of the model. The threshold values for the voltage, along with uso and ucsi, were constrained to vary between the minimum and maximum value of the membrane potential (0 and 1, respectively). The diffusion constant was allowed to vary between 10-5 and 0.1 cm^2/ms, but none of the fits were more than an order of magnitude away from 0.001 cm^2/ms. In order to incorporate the range of possible values given in the parameter sets of Ref. [FCHE02] all remaining parameters were allowed to vary over several orders of magnitude.

A.1.3 Curve-fitting procedure

Two points along the 1D cable, consisting of 100 elements, were used to compute the fit to clinical data. Specifically, we used element N=70 for the APD and AP morphology fits and used element N=30 and N=70 to calculate the CV. We have verified that these points were sufficiently far from the boundaries to minimize boundary effects. The cable was stimulated at one end using an S1/S2 protocol similar to the one used in the patients, where S1=500 ms was repeated 5 times before each S2 stimulus. Before each fitting iteration we stimulated the cable 30 times with CL=500 ms to ensure that the model had reached a steady state. For each patient, 10 S2 values were chosen such that the resulting DI, determined as the time interval between the end of the preceding AP and the time of the S2 stimulus, falls into the clinical DI range (DImin to DImax). The numerical algorithm then produces simulation data for the AP morphology, and for the APD and CV restitution curves, which can be simultaneously fitted to clinical data. Accuracy of the fit was defined through an error function which measures the discrepancy of the numerical results and the clinical data as follows:

$$E = \frac{1}{M}\Sigma_{i=1}^{M}\frac{|x_i^{sim} - x_i^{clin}|}{(x_i^{clin}} \tag{A.8}$$

where and are the values of the simulation and clinical data points, respectively, and where

M is the total points that are used in the error function. Here, we have chosen M=30 such that, as detailed below, each clinical data set contributes 10 points. The task of the fitting procedure is to search for the parameter set k that minimizes E. AP morphology fits for the KKT model were calculated by choosing 10 evenly spaced points along the AP curve generated by the model and comparing them to the corresponding points of the polynomial function derived from clinical data. Since the MAP recordings did not capture the initial phase of the AP, we did not fit the AP upstroke and set the rescaled potential to 1 at t=0. This was performed for each of the 10 S2 stimuli and the error functions was averaged over all S2 values. Since the clinical AP morphology was largely independent of the S2 value (Fig. 2.1) we rescaled the clinical AP shape to adjust to the required APD value. For both the APD and CV restitution curves, we compared the numerical value of APD and CV to the one obtained from the polynomial fits of the clinical data. At the start of the fits, we chose S2 stimuli that were equally distributed in the clinical range. After manually inspecting the obtained fits, the DI values were adjusted to ensure better fits in parts of the restitution curves that were not optimally captured by the parameter sets. This typically meant a larger emphasis on the lower than on higher DI values. The fitting procedure for the FK model incorporated the same conditions as described above but also used upstroke times obtained in the KKT fits. Specifically, for each S2 in the KKT morphologies we determined the time interval t between 10% and 100% of the upstroke amplitudes (Fig. A.3). This time interval was then used as an additional condition for the FK fitting procedure and ensures similar upstroke morphologies in both models.

A.2 CV data for the remaining patients

The raw conduction velocity data as a function of cycle length was shown for patient three in Chapter 2. Here, Figure A.1 shows the plots of the remaining four patients for completeness. As discussed in the main text, the plots of conduction velocity vs. cycle length were converted

into plots of conduction velocity vs. diastolic interval. From there, the data was fit to a polynomial function as shown in Figure A.2.

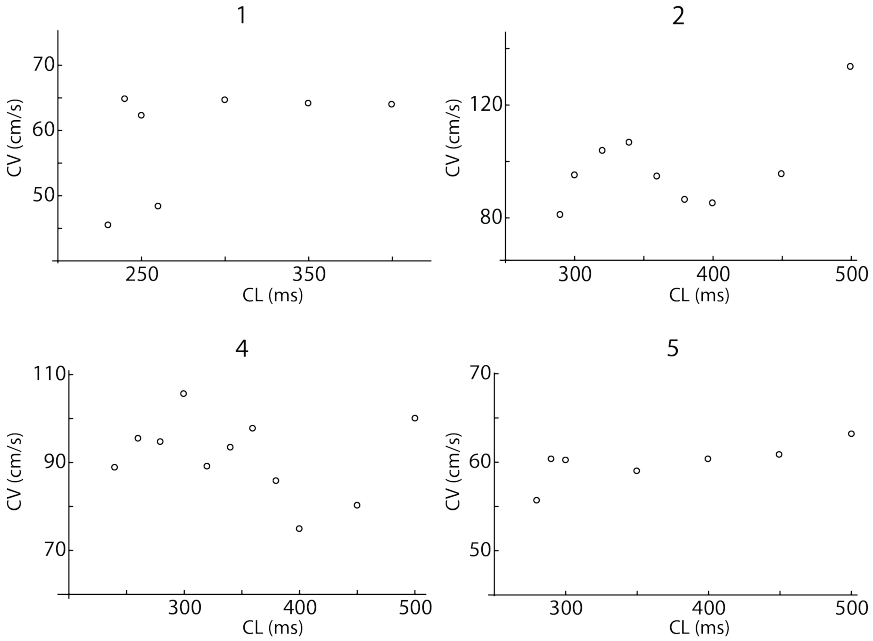

Figure A.1: Shown is the CV as a function of CL for patients 1, 2, 4, and 5. The equivalent curve for patient 3 is shown in Chapter 2.

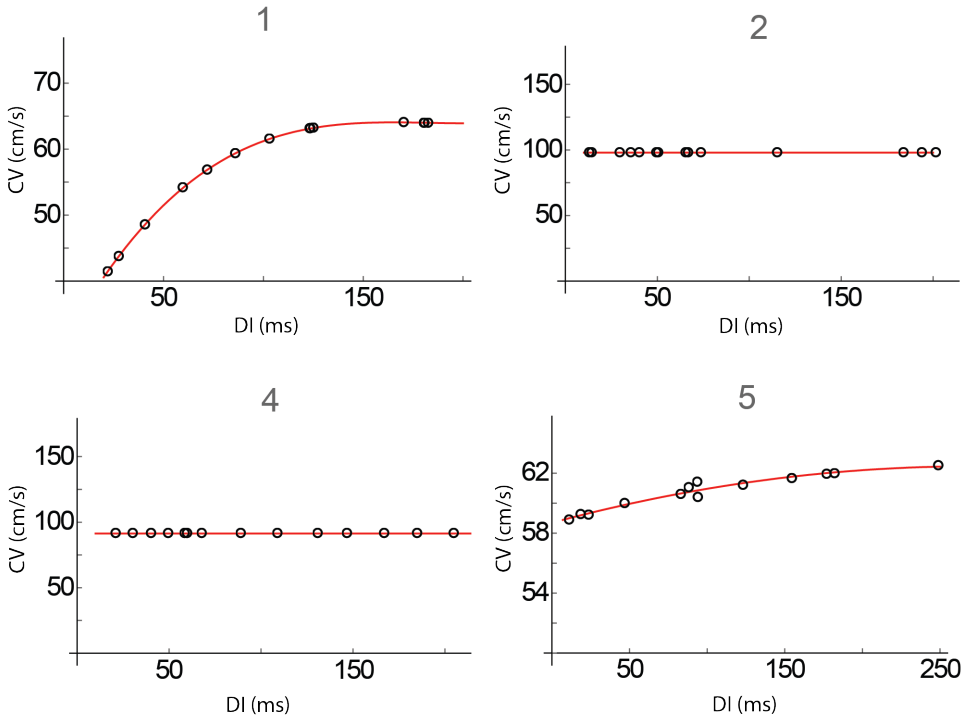

Figure A.2: Shown is the CV as a function of DI for patients 1, 2, 4, and 5. The equivalent curve for patient 3 is shown in Chapter 2.

A.3 Upstroke of the FK and KKT models

The time interval t between 10% and 100% of the upstroke amplitudes of the KKT model was used as additional fit condition for the FK model. Figure A.3 shows the results for the largest DI value.

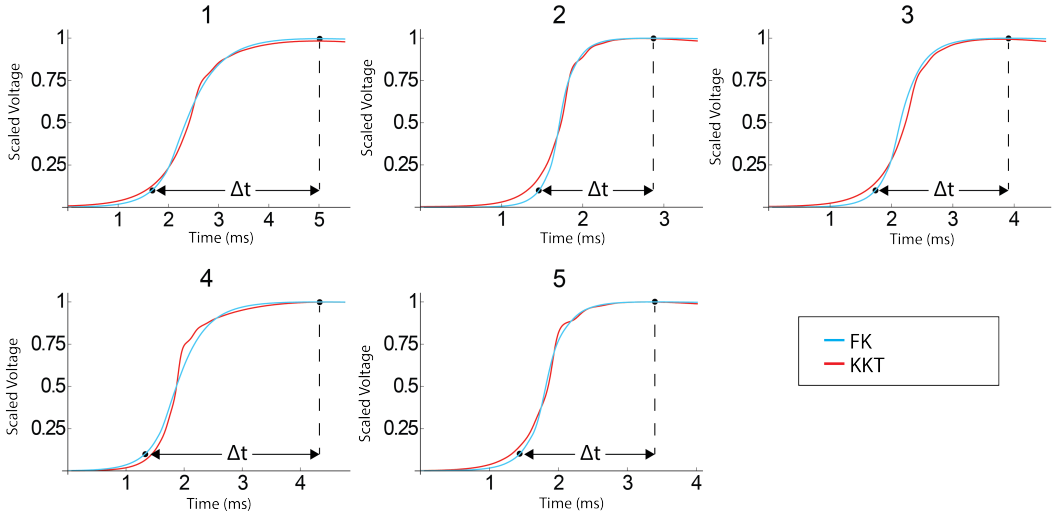

Figure A.3: The upstroke part of the APs obtained from the KKT fits are shown in red while the corresponding AP shapes of the FK model are shown in blue.

A.4 Model Parameters

The KKT model discussed in Chapter 2 includes numberous parameters. When fitting to the patient data, only the parameters shown in Table A.1 were adjusted. The remaining parameters were fixed at the values given in the original text. The final resulting parameters for each patient are shown in Table A.2. Likewise, the fitted parameters for the FK model are shown in Table A.3. For completeness, the original paramater values for the KKT and FK models are shown in Tables A.4 and A.5 respectively.

Chapter 2 also discusses the possibility using more parameters in the fit of the KKT model, but it is found that this does not improve the fit. For completeness, the values found from fitting 32 parameters of the KKT model to data from patient 1 are shown in Table A.6. Finally, it is worth noting that these fits to the data are not unique. Tables A.2 and A.3 both show alternate parameters that fit equally as well to patient one. To further demonstrate this point, we refit five parameters of the KKT model to the original AP and APD curves made by the published parameters. Table A.7 shows four alternate parameter sets that closely reproduce the AP and APD curves found by the original parameters of the model.

Table A.1: Parameters of the KKT model used for fitting to patient data.

Parameter	Description
BCa	Ca buffer concentration (mM)
K_{dBCa}	Dissociation constant (mM)
P_{Na}	Permeability of INa (nL/s)
E_{Ca_app}	Apparent Reversal Potential for ICaL (mV)
$kCan$	Exponential factor in CaL time constant
k_{Ca}	Half max Ca in L-type current (mM)
g_{Ks}	Conductance value for IKs (nS)
g_{K1}	Conductance value for IK1 (nS)
g_{Nab}	Conduction value for background Na (nS)
g_{Cab}	Conduction value for background Ca (nS)
$I_{ICaPmax}$	Max Ca pump current (pA)
k_{CaP}	Half max Ca binding concentration (mM)
γ	Position of energy barrier controlling voltage dependence of INaCa
d_{NaCa}	Coefficient in INaCa $(mmol/L)^{-4}$
D_{Ca}	Ca diffusion coefficient $(\mu m^2/s)$
D_{CaSR}	Ca diffusion in SR region $(\mu m^2/s)$
D_{CaBm}	Ca diffusion in buffer $(\mu m^2/s)$
D_{Na}	Na diffusion coefficient $(\mu m^2/s)$
k_4	pump rate from SERCA to SR (s^{-1})
k_{SRleak}	SR leak scaling parameter (s^{-1})
D (diffusion)	diffusion between cells (cm^2/ms)

Table A.2: Parameter values of the KKT model obtained by fitting for all 5 patients.

Parameter	1	1 Alt.	2	3	4	5
BCa	0.07488	8.113E-03	0.04279	0.07364	0.01963	0.02143
K_{dBCa}	9.716E-04	2.065E-03	3.393E-03	2.382E-03	2.166E-03	1.806E-03
P_{Na}	2.141E-03	2.370E-03	6.411E-03	2.920E-03	6.380E-03	4.580E-03
E_{Ca_app}	91.26	45.95	60.86	46.92	286.5	75.24
$kCan$	1.051	0.8541	1.432	0.5913	1.085	1.100
k_{Ca}	3.848E-04	6.056E-04	1.328E-03	4.955E-04	2.088E-04	8.424E-04
g_{Ks}	0.6346	0.3174	0.7901	0.7217	9.312	1.453
g_{K1}	6.255	5.256	3.890	2.634	2.225	4.353
g_{Nab}	0.1224	0.1095	0.01034	0.05286	8.472E-03	0.08860
g_{Cab}	0.09949	0.09934	0.06184	0.05006	0.01022	0.09369
$I_{ICaPmax}$	3.365	0.7689	1.271	2.472	0.2239	4.219
k_{CaP}	9.420E-04	2.133E-04	4.120E-03	1.248E-03	2.603E-03	8.411E-04
γ	0.5941	0.7096	0.4043	0.6359	0.04726	0.2300
d_{NaCa}	4.671E-05	1.127E-04	3.352E-05	1.291E-04	1.315E-04	8.072E-05
D_{Ca}	166.4	1927	327.3	467.8	7076	871.6
D_{CaSR}	54.30	6.212	98.19	78.69	41.34	59.84
D_{CaBm}	71.55	38.25	88.32	49.71	131.3	29.72
D_{Na}	0.4046	0.4908	0.07802	0.1427	0.1522	0.08442
k_4	6.813	119.5	6.806	5.587	10.38	3.880
k_{SRleak}	3.073E-03	0.02863	2.632E-03	0.02296	0.04236	3.789E-03
D (diffusion)	2.164E-03	1.945E-03	2.413E-03	2.785E-03	2.127E-03	1.209E-03

Table A.3: Parameter values of the FK model obtained by fitting for all 5 patients.

Parameter	1	1 Alt.	2	3	4	5
u_c	0.1313	0.2171	0.2579	0.2131	0.2069	0.2588
u_v	0.3085	0.1142	0.1799	0.1107	0.03489	0.1382
u_w	0.2635	0.2508	0.2566	0.2798	0.1788	0.2589
u_d	0.05766	0.1428	0.1943	0.1601	3.140E-04	0.1797
t_v^-(ms)	57.12	46.77	40.31	35.75	971.3	45.15
t_v^+(ms)	2.189	1.759	1.349	1.247	2.243	2.194
t_w^-(ms)	68.50	80.18	89.08	109.8	110.7	166.4
t_w^+(ms)	871.4	749.5	777.0	751.8	616.0	836.3
t_s^+(ms)	1.110	1.484	1.144	1.487	16.29	1.315
t_s^-(ms)	1.7570	1.983	1.086	2.241	7.104E-03	0.764
u_{csi}	0.1995	0.2168	0.2722	0.2097	0.1682	0.2023
x_k	6.043	21.62	6.142	8.679	8.958	7.351
$t_d(ms)$	0.12990	0.08673	0.04456	0.06880	0.08511	0.06711
$t_o(ms)$	15.17	17.05	23.45	18.31	6.754	18.28
$t_{soa}(ms)$	72.66	54.90	97.89	54.43	152.9	105.4
$t_{sob}(ms)$	7.933	1.685	3.308	4.894	19.82	3.264
u_{so}	0.4804	0.6520	0.4185	0.6804	6.013E-03	0.3497
x_{tso}	2.592	2.161	1.997	2.187	8.677	1.968
t_{si}(ms)	40.11	38.82	36.60	40.39	18.94	39.23
$D(cm^2/ms)$	1.611E-03	1.337E-03	1.405E-03	1.704E-03	2.696E-03	8.479E-04
t_{v2}^-(ms)	1012	1321	1183	1187	120.5	1166

Table A.4: Parameter values of the KKT model from the original published paper

Parameter	orignal value
BCa	0.02400
K_{dBCa}	2.380E-03
P_{Na}	1.800E-03
E_{Ca_app}	60.00
$kCan$	2.000
k_{Ca}	6.000E-04
g_{Ks}	1.000
g_{K1}	3.450
g_{Nab}	0.06060
g_{Cab}	0.09520
$I_{ICaPmax}$	2.000
k_{CaP}	5.000E-04
γ	0.4500
d_{NaCa}	3.000E-04
D_{Ca}	780.0
D_{CaSR}	44.00
D_{CaBm}	25.00
D_{Na}	0.1200
k_4	13.00
k_{SRleak}	6.000E-03
D (diffusion)	1.000E-03

Table A.5: Parameter values of the FK model from the original published paper

Parameter	orignal value
u_c	0.1300
u_v	0.04000
u_w	0.1300
u_d	0.1300
t_v^-(ms)	19.60
t_v^+(ms)	3.330
t_w^-(ms)	41.00
t_w^+(ms)	870.0
t_s^+(ms)	1.000
t_s^-(ms)	1.000
u_{csi}	0.8500
x_k	10.00
$t_d(ms)$	0.2500
$t_o(ms)$	12.50
$t_{soa}(ms)$	33.30
$t_{sob}(ms)$	33.30
u_{so}	0.8500
x_{tso}	10.00
t_{si}(ms)	29.00
$D(cm^2/ms)$	1.000E-3
t_{v2}^-(ms)	1250

Table A.6: Parameter values of the KKT model obtained by fitting 32 parameters to data from patient 1.

Parameter	Value
BCa	0.07825
K_{dBCa}	9.926E-04
P_{Na}	2.169E-03
E_{Ca_app}	89.83
$kCan$	1.051
k_{Ca}	3.810E-04
g_{Ks}	0.5992
g_{K1}	6.334
g_{Nab}	0.1218
g_{Cab}	0.09771
$I_{ICaPmax}$	3.281
k_{CaP}	9.287E-04
γ	0.6117
d_{NaCa}	4.497E-05
D_{Ca}	165.0
D_{CaSR}	58.34
D_{CaBm}	81.61
D_{Na}	0.3983
k_4	7.093
k_{SRleak}	2.826E-03
D (diffusion)	2.149E-03
B_{Na}	1.050
Kd_{BNa}	9.569
k_{NaCa}	9.025E-03
$INaK_{max}$	71.28
k_{NaKK}	0.9785
k_{NaKNa}	11.26
g_t	8.242
g_{sus}	2.244
g_{Kr}	0.4762
g_{CaL}	14.86
g_{If}	1.061

Table A.7: Parameter values of the KKT model obtained by fitting 5 parameters to simulated AP and APD data produced by the original data set.

Parameter	Value				
P_{Na}	1.734E-03	1.778E-03	1.762E-03	1.780E-03	1.800E-03
g_{Ks}	0.5437	1.462	1.104	0.6031	1.000
g_{K1}	3.614	3.401	3.543	3.410	3.450
g_{Cab}	0.09056	0.09498	0.09122	0.09897	0.09520
g_{Nab}	0.07642	0.06127	0.07521	0.04710	0.06060

Appendix B

Appendix to Chapter 3

B.1 Detailed Methods

The method used in this paper was first developed by Transtrum and Qiu [TQ14] and is referred to as the Manifold Boundary Approximation Method (MBAM). Here, we outline in more detail how we applied this approach to the atrial myocyte model developed by Koivumaki et al. [KKT11, KSMT14]

A model with N parameters $(\theta_1, \theta_2, ..., \theta_N)$ can be described as an N-dimensional parameter space manifold that is embedded within an M-dimensional data space. The coordinates of the manifold in data space represent the measured quantities of the variables, $(y_1, y_2, ..., y_M)$. The point along the surface of the manifold that is closest to the desired data point, $(Y_1, Y_2, ..., Y_M)$, represents the best fit of the model. This can be found by minimizing the cost function:

$$C = \sum_{m=1}^{M} \frac{1}{2}(y_m - Y_m)^2. \tag{B.1}$$

For the purpose of this paper, the Koivumaki Korhonen Tavi (KKT) model had 37 different parameters with 42 variables. As we are only concerned with the action potential shape, the measured quantities are 60 time points at which the membrane potential was recorded. Thus,

the measured quantities of the model are the voltage at each of the chosen time points, $V(\vec{\theta}, t_m)$. The data points, in this case, are the original values of the published model, $V(\vec{\theta}^*, t_m)$. The cost function can then be written as:

$$C = \sum_{m=1}^{M} \frac{1}{2}(V(\vec{\theta}, t_m) - V(\vec{\theta}^*, t_m))^2. \tag{B.2}$$

The MBAM method uses information about the structure of the parameter space manifold to reduce the number of parameters. In many biophysical models, there exist parameters which can vary over a wide range of values without greatly effect the measured quantities of the model. These have been defined as sloppy parameters [BS03b]. The parameter space manifold can be extremely narrow in directions that are very sloppy, and very wide in directions that are stiff. This is not limited to single parameters, as there can also be combinations of parameters that lead to sloppy directions on the manifold as well.

Given a starting coordinate on the parameter manifold, we want to reduce the dimensionality without greatly affecting the cost at our initial position. That is, we want to reduce the model without changing the values of the measured quantities. This is accomplished by looking for the boundary of the manifold that is closest to our starting coordinate, corresponding with the sloppiest direction, and then approximating the model at this boundary.

To begin this process, we find the sloppy directions on the manifold by calculating the Hessian Matrix, H:

$$H_{i,j} = \frac{\partial}{\partial \theta_i}\frac{\partial}{\partial \theta_j} C. \tag{B.3}$$

This can be approximated by ignoring the second derivative terms [TMS11] :

$$H_{i,j} \approx (\frac{\partial}{\partial \theta_i} V(\vec{\theta}, t_m))(\frac{\partial}{\partial \theta_j} V(\vec{\theta}, t_m)). \tag{B.4}$$

This is also known as the metric, g, of the parameter space manifold. From our starting point in parameter space, the eigenvalues of the metric are a measure of the distance that can be traveled without significantly changing the measured results for the model. The smallest eigenvalue corresponds with the boundary closest to the starting point. However, with the KKT model these terms cannot be solved for analytically. We do not have an expression for $V(\vec{\theta}, t_m)$, so instead we numerically integrate

$$\frac{\partial}{\partial \theta_\mu} \frac{dV(\theta, t_m)}{dt} = \frac{\partial}{\partial \theta_\mu} \frac{I_{ion}(\theta)}{-C_m}. \tag{B.5}$$

The term I_{ion} is the sum of all the ionic currents in the model. Since this term will depend on the other equations within the model, we must take the derivative and numerically integrate all of the equations in the model. Derivatives with respect to the parameters were performed in Mathematica 10. Numerical integration was done with a forward euler scheme using C++, with a time step of 0.01ms. It should also be noted that the numerial integration requires values to be given for each of the parameters. This means that the metric tensor really only applies to the local region around the chosen point on the parameter space manifold. Yet we still have some global knowledge of the parameter space by knowing the values of the boundaries for each of the parameters. In our case, these starting parameters were the original published values of the KKT model. From here, the MBAM method was used to evolve the parameters towards the nearest boundary, and reduce the model.

Once the nearest boundary is found, a procedure is necessary for how the model should approach it. In order to minimize the change in the model's results, as the coordinates are moved from the starting point to the boundary, the model should advance along the geodesic of the manifold. The change in the coordinates is given by the geodesic equation:

$$\ddot{\theta}^\mu + \Gamma^\mu_{\alpha\beta} \dot{\theta}^\alpha \dot{\theta}^\beta = 0. \tag{B.6}$$

Einstein summation convention is used here, indicating that repating indices are summed over all values. The dot notation used in these equations represents the derivative with respect to the affine parameter of the geodesic. The terms $\Gamma^{\mu}_{\alpha\beta}$ are known as the connection coefficients. Transtrum and Qiu note that these can be estimated as

$$\Gamma^{\mu}_{\alpha\beta} = g^{\mu\nu}\Sigma_{m=1}^{N}\partial_{\nu}V(t_m)\partial_{\alpha}\partial_{\beta}V(t_m). \tag{B.7}$$

The second-derivative componenet is calculated using a finite difference method along with the first derivatives that were calculated for the Jacobian matrix. Next, the product of the inverse metric, $g^{\mu\nu}$, and the first derivative term, $\partial_{\nu}V(t_m)$, can be solved for using the matrix equation [TS12]:

$$g_{\mu\nu}\vec{b} = J_m^T.$$

$$\vec{b} = g^{\mu\nu}J_m^T. \tag{B.8}$$

The NVIDIA cuSolver library is used to calculate the eigenvalues and eigenvectors, and for calculating the connection coefficients. The geodesic equation is then numerically integrated by defining $\phi = \dot{\theta}$ and using a forward euler scheme to solve the system:

$$\dot{\phi}^{\mu} + \Gamma^{\mu}_{\alpha\beta}\phi^{\alpha}\phi^{\beta} = 0. \tag{B.9}$$

$$\dot{\theta}^{\mu} = \phi^{\mu}. \tag{B.10}$$

The initial value of $\vec{\phi}$ is the eigenvector that corresponds with the smallest eigenvalue. An adaptive time step was used for the numerical integration.

B.2 Adjustment to L-Type Calcium Current

During one of the last iterations of the reduction algorithm it was found that, at the limit, the gating variable I_{CaLfca} could be clamped to one as k_{Can} went towards infinity.The original equations for the current are:

$$\frac{\partial I_{CaLfca}}{\partial t} = (I_{CaLfca\,\mathrm{inf}} - I_{CaLfca})/I_{CaLfca\tau}. \tag{B.11}$$

$$I_{CaLfca\,\mathrm{inf}} = 1 - 1/(1 + (k_{Ca}/[Ca]_{ss})^{k_{Can}}). \tag{B.12}$$

$$I_{CaL} = g_{CaL} * I_{CaLd} * I_{CaLfca} * I_{CaLf2} * (V - E_{Ca_app}). \tag{B.13}$$

At another step, E_{Ca_app} increased to infinity, while g_{CaL} decreased to 0. This reduced the current equation to depend on the parameter ϕ_{CaL}, which is the product of the conductance and effective reversal potential. The final result is:

$$I_{CaL} = -\phi_{CaL} * I_{CaLd} * I_{CaLf2}. \tag{B.14}$$

The equations for I_{CaLd} and I_{CaLf2}. remain unchanged, along with the remaining currents and concentrations, but are given below for completeness. Further information can be found in the publication for the detailed model [KSMT14]:

$$\frac{\partial I_{CaLd}}{\partial t} = (I_{CaLd\,\mathrm{inf}} - I_{CaLd})/I_{CaLd\tau}. \tag{B.15}$$

$$\frac{\partial I_{CaLf2}}{\partial t} = (I_{CaLf2\,\mathrm{inf}} - I_{CaLf2})/I_{CaLf2\tau}. \tag{B.16}$$

$$I_{Na} = P_{Na} * (I_{Nam})^3 * (0.9 * I_{Nah1} + 0.1 * I_{Nah2}) * Na_o * V * \frac{F^2}{R*T} * \frac{e^{(V-E_{Na})*F/(R*T)} - 1}{e^{V*F/(R*T)} - 1}. \quad \text{(B.17)}$$

$$\frac{\partial I_{Nam}}{\partial t} = (I_{Nam\,\inf} - I_{Nam})/I_{Nam\tau}. \quad \text{(B.18)}$$

$$\frac{\partial I_{Nah1}}{\partial t} = (I_{Nah1\,\inf} - I_{Nah1})/I_{Nah1\tau}. \quad \text{(B.19)}$$

$$\frac{\partial I_{Nah2}}{\partial t} = (I_{Nah2\,\inf} - I_{Nah2})/I_{Nah2\tau}. \quad \text{(B.20)}$$

$$I_t = g_t * I_{tr} * I_{ts} * (V - E_K). \quad \text{(B.21)}$$

$$\frac{\partial I_{tr}}{\partial t} = (I_{tr\,\inf} - I_{tr})/I_{tr\tau}. \quad \text{(B.22)}$$

$$\frac{\partial I_{ts}}{\partial t} = (I_{ts\,\inf} - I_{ts})/I_{ts\tau}. \quad \text{(B.23)}$$

$$I_{sus} = g_{sus} * I_{susr} * I_{suss} * (V - E_K). \quad \text{(B.24)}$$

$$\frac{\partial I_{susr}}{\partial t} = (I_{susr\,\inf} - I_{susr})/I_{susr\tau}. \quad \text{(B.25)}$$

$$\frac{\partial I_{suss}}{\partial t} = (I_{suss\,\inf} - I_{suss})/I_{suss\tau}. \quad \text{(B.26)}$$

$$I_{K1} = g_{K1} * (K_o)^{0.4457} * (V - E_K)/(1 + e^{1.5(V - E_K + 3.6) * F/(R * T)}). \tag{B.27}$$

$$\frac{\partial K_i}{\partial t} = (I_t + I_{sus} + I_{K1} + I_{stim})/(V_{cytosol} * F). \tag{B.28}$$

$$\frac{\partial V}{\partial t} = -(I_{Na} + I_{CaL} + I_t + I_{sus} + I_{K1} + I_{stim})/C_m. \tag{B.29}$$

B.3 Action Potential Data Points

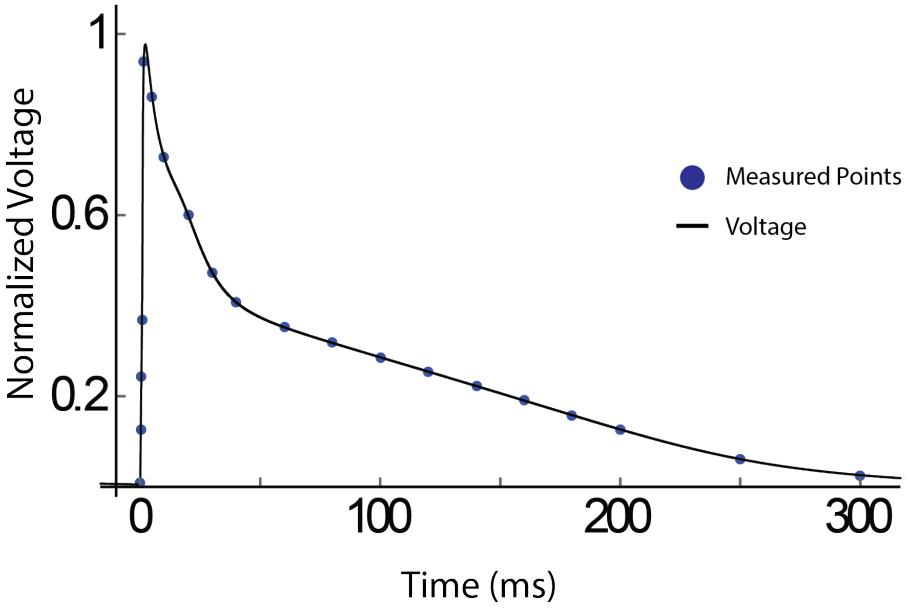

Figure B.1: Twenty points along the AP shape were chosen for each of the three S2 stimuli that were applied during the pacing protocol. These points were chosen to represent the upstroke, repolarization, and resting state of the model.

B.4 Variable Changes Between Iterations

In addition to the parameter changes shown in Chapter 3, there are also reductions to the number of time dependent variables as well. Figure B.2 shows the specific changes made for each reduced model presented in Chapter 3. Of particular note are the intracellular calcium and sodium concentrations. The intracellular calcium concentrations were not needed in the R_{final} model, as all the dependent currents were already removed. In the final step, the intracellular sodium concentrations were combined into a single term, and held constant. Allowing this final sodium concentration to vary would cause it to slowly leak out, as the I_{Na} current is the only dependent term remaining in the final model that affects it. This constant value could be added as a fitting parameter for the model, but this was not necessary for the results shown in the main text. Instead, the average value of Na_{ss} and Na_i can be used as the new constant for the sodium concentration.

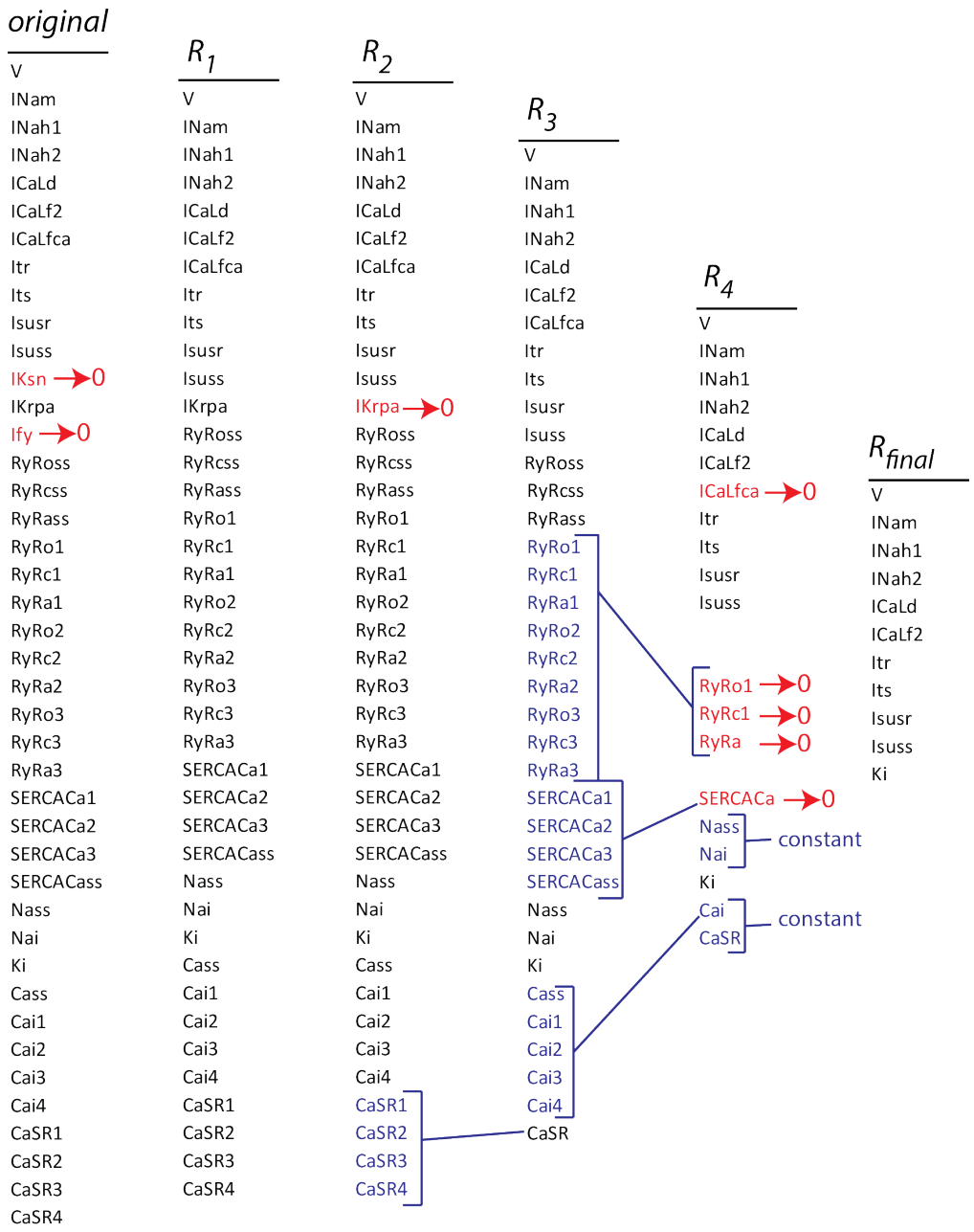

Figure B.2: All variables for each of the models. Variables that are highlighted in red are removed in the next model. Variables highlighted in blue were combined to form new variables in the next model.

B.5 Extended APD Restitution Curve

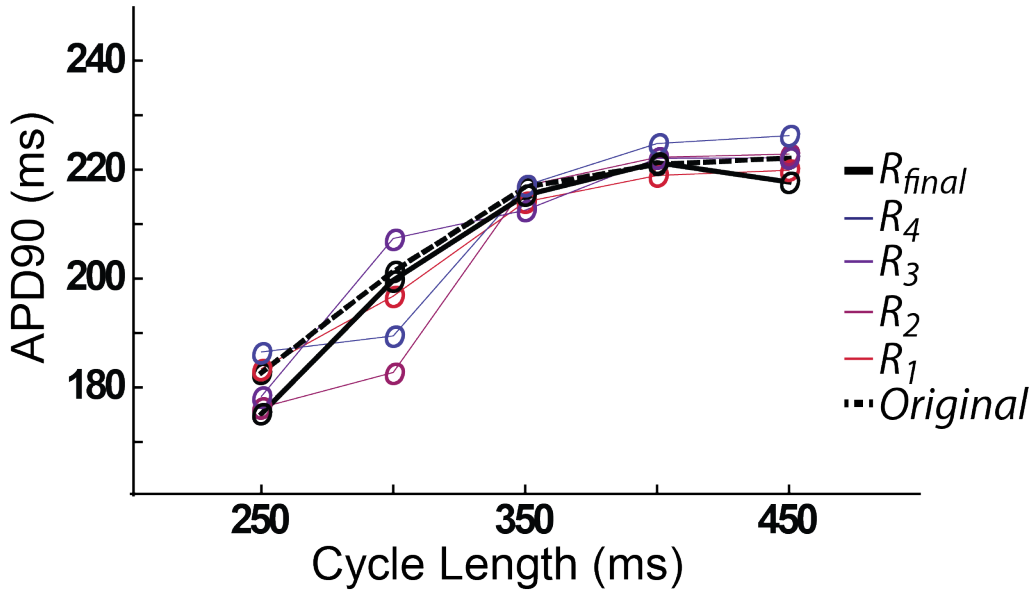

Figure B.3: APD restitution curve for each of the models using 5 different S2 stimuli. This differs from the protocol used during the reduction and fitting algorithms, which only had 3 S2 stimuli.

B.6 APD Stability of Each Model.

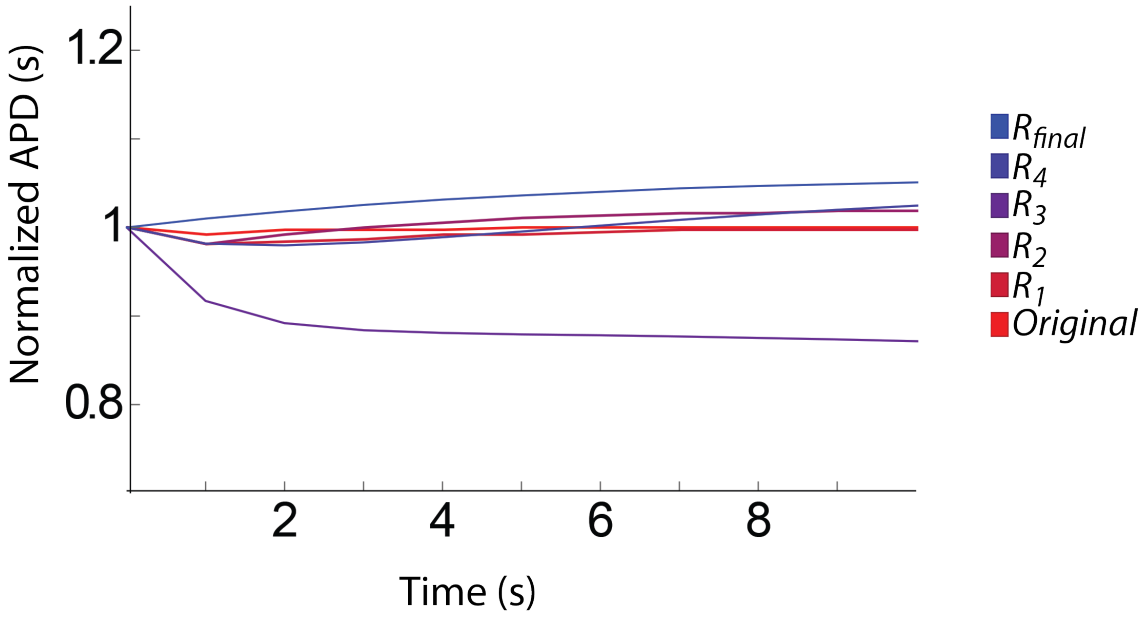

Figure B.4: Each model was paced for 10s at a cycle length of 1s. The APD value of each stimulus was normalized with respect to the first stimulus.

B.7 Spiral Wave Generation from Reduced Model

The images shown are for a 200x200 element grid, with a spatial discretization of 0.02cm. The diffusion constant is set to $0.001 cm/s^2$. Initially, the first five columns on the left of the sheet were stimulated, followed by a second stimulus applied to the center of the grid at a later time (296ms for the reduced model, and 275ms for the original model). The screenshots show the membrane potential at 50 and 100ms after the second stimulus was applied.

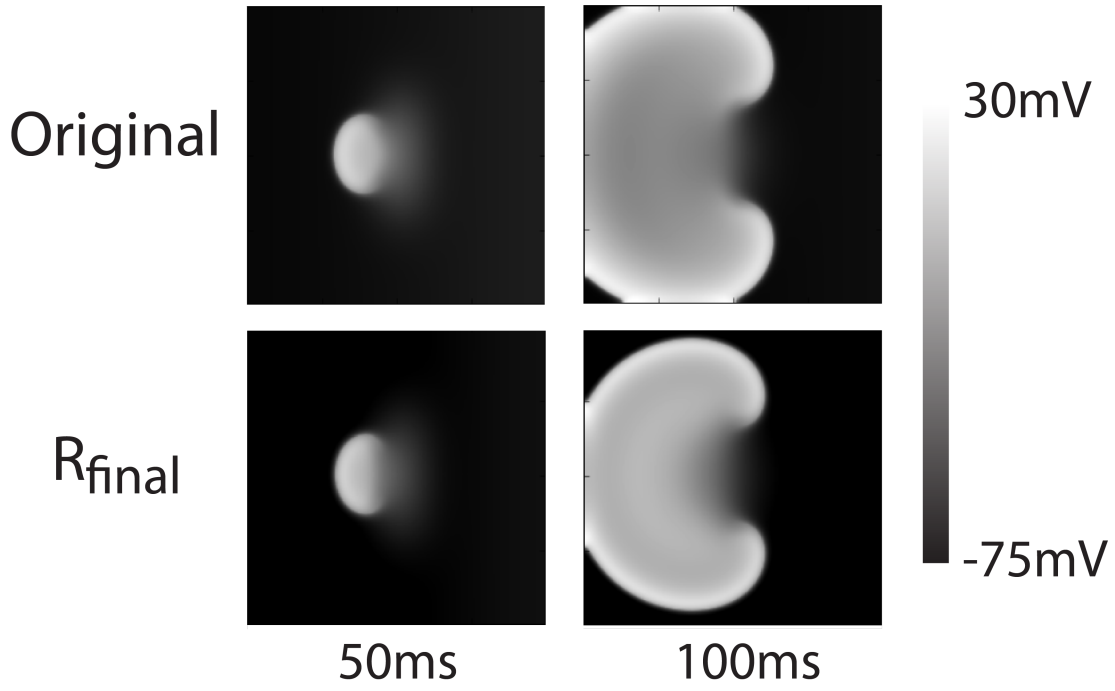

Figure B.5: Snapshots of a 2D simulation on a homogeneous domain for the final reduced model (lower panels) and the original model (upper panels) for comparison.

B.8 Parameter Values for Each of the Models.

Original	
BCa	2.40E-02
KdBCa	2.38E-03
PNa	0.0018
ECa_app	60
kCan	2
kCa	6.00E-04
gKs	1
gK1	3.45
gNab	0.060599
gCab	0.0952
ICaPmax	2
kCaP	0.0005
gam	0.45
dNaCa	0.0003
DCa	780
DCaSR	44
DCaBm	25
gIf	1
DNa	0.12
k4	13
kSRleak	6.00E-03
gCaL	15
gt	8.25
gsus	2.25
gKr	0.5
kNaCa	0.0084
CSQN	6.7
KdCSQN	0.8
BNa	1.1319
KdBNa	10
INaKmax	70.8253
kNaKK	1
kNaKNa	11
SLLow	165
SLhigh	13
KdSLlow	1.1
KdSLhigh	1.30E-02

i_1	
BCa	0.020177
KdBCa	0.002457
PNa	0.001766
ECa_app	60.76713
kCan	1.708886
kCa	0.000728
gK1	3.829988
gNab	0.057762
gCab	0.108181
ICaPmax	1.902651
kCaP	0.000514
gam	0.44192
dNaCa	0.000282
DCa	791.9988
DCaSR	50.48111
DCaBm	17.10939
DNa	0.128977
k4	13.6667
kSRleak	0.006046
gCaL	14.6364
gt	7.4139
gsus	2.767606
gKr	0.600335
kNaCa	0.007763
INaKmax	66.34891
kNaKNa	12.78808
SLLow	166.8345
SLhigh	14.18246
KdSLlow	0.942645
KdSLhigh	0.013539

i_2	
PNa	0.001836
ECa_app	59.51315
kCan	4.77848
kCa	0.000777
gK1	3.751993
gCab	0.116835
gam	0.55132
dNaCa	0.002341
DCa	848.3585
DCaSR	237.6186
DNa	0.090966
k4	9.312152
gCaL	9.062336
gt	7.864459
gsus	1.738592
gKr	1.357176
kNaCa	0.056333
INaKphi	0.515589
SLLow	463.7933
SLhigh	13.58182
KdSLlow	2.053872
KdSLhigh	0.011729

i_3	
PNa	0.001587
ECa_app	84.71477
kCan	0.6344
kCa	0.000208
gK1	3.385621
gCab	0.062882
DCa	5050.036
DNa	0.102608
k4	13.0084
gCaL	24.30867
gt	9.07595
gsus	3.986455
INaCaphi	6.091821
SLLow	176.1608
SLhigh	12.66392
KdSLlow	0.714543
KdSLhigh	0.009825

i_4	
PNa	0.001519
phiCaL	556.1077
gK1	1.367415
gCab	0.018166
DNa	0.006
k4	5.441145
gt	15.46703
gsus	2.185673
INaCaPhi	2.917834

i_{final}	
PNa	0.00131
phiCaL	648.1718
gK1	1.121406
gt	14.30201
gsus	3.22985

Figure B.6: final parameter values used for each of the reduced models.

Appendix C

Appendix To Chapter 4

C.1 Numerical analysis

Our simulations were performed on a two dimensional square sheet with a spatial discretization of 0.025 cm and a side length of 200 elements (Fenton-Karma (FK) model) or 400 elements (Koivumäki, Korhonen, and Tavi (KKT) model) and no-flux boundary conditions. The time step was chosen to be 0.05 ms and 0.01 ms for the FK and KKT model, respectively. We used the Cuda Parallel Computing platform to calculate each grid element simultaneously, resulting in very efficient computational algorithms. Numerical integration was performed using the forward Euler method, and we simulated a 60s time segment. In order to allow the system to reach a steady state, only the last 30s of the simulation were recorded. The coordinates of the tip trajectory were saved every 5 ms. We have verified that the results did not significantly change if the time step was lowered by a factor of 5.

As there are many versions of Fenton-Karma model, the equations used for the results in this paper are presented here. The equations for the gating variables (v,w) and the currents (I_{fi}, I_{so}, I_{si}) are:

$$\frac{dv}{dt} = \frac{(1-\mathcal{H}(u-V_c))(1-v)}{(1-\mathcal{H}(u-V_v))\tau_{v1}^{-} + \mathcal{H}(u-V_v)\tau_{v2}^{-}} - \frac{\mathcal{H}(u-V_c)v}{\tau_v^{+}}. \tag{C.1}$$

$$\frac{dw}{dt} = \frac{(1-\mathcal{H}(u-V_c))(1-w))}{\tau_w^{-}} - \frac{\mathcal{H}(u-V_c)w}{\tau_w^{+}} \tag{C.2}$$

$$I_{fi} = -\frac{\mathcal{H}(u-V_c)(u-V_c)(1-u)v}{\tau_d} \tag{C.3}$$

$$I_{so} = \frac{u(1-(u-V_c))}{\tau_o} + \frac{\mathcal{H}(u-V_c)}{\tau_r} \tag{C.4}$$

$$I_{si} = -w\frac{1+\tanh(k(u_i-V_c^{si}))}{2*\tau_{si}} \tag{C.5}$$

C.2 Model Parameter Values

The parameters for Set I and Set II of the Fenton-Karma model [FCHE02] used in our study are listed in Table S1. The excitability of the fast inward current in the circular, heterogeneous regions was decreased by raising the value of the parameter τ_d to 0.5ms. The parameters for the KKT model, based on the most recently published values [KSMT14], are given in Table S2. Within the heterogeneous regions, the value of P_{Na} in the sodium channel I_{Na} was set to half of its original value.

C.3 Method of Estimating Lyapunov Exponent

As a measure of chaos for each of the spiral trajectories in the two models, the dominant Lyapunov exponent was estimated using a procedure developed by Wolfe et. al [WSSV85]. This exponent is a measure of how many bits of information are lost per second of simulation time and a positive value of λ indicates that the dynamics is chaotic. We used a publicly available Matlab version of this procedure. First, an attractor is constructed from delay coordinates of the time series of the tip trajectory. The Lyapunov exponent is then approximated by looking at two nearby points in the phase space and observing how the distance between them changes as the system evolves. If the separation grows past a given tolerance, then a new set of points is chosen and the process is repeated. A more detailed description of the method can be found in both the original paper, and the documentation for the Matlab code.

Both 4- and 3-dimensional delay coordinates were used for calculating the dominant exponent, as recommended in the original paper. It was found that the results did not significantly vary between the two, and so all values are reported with the 4-dimensional delay coordinates. The time delay was set to be approximately equal to 1/3 the orbital period, and varies for different configurations. The tolerance level for the distance, determining when to stop the comparison between two points and choose a new set, is set to be between $10-15\%$ of the spatial extent of the x-coordinate of the tip trajectory. For all simulations shown here, the tip position is recorded once every 5 ms, giving approximately 20 to 50 points per orbit. The final output of the Lyapunov exponent is given in units of bits/second. This is then an indication of how many bits of information are lost each second of the simulation.

C.4 Analytic solution for the particle model

For the specific case of homogeneous media, the equations for the SP model become analytically solvable.

$$x(t) = -\frac{e^{-\xi t}}{\xi} C_{1x} + C_{2x} + F_1 \frac{\xi \sin(\omega_1 t + \phi) - \omega_1 \cos(\omega_1 t + \phi)}{\omega_1(\xi^2 + \omega_1^2)} + F_2 \frac{\xi \sin(\omega_2 t) - \omega_2 \cos(\omega_2 t)}{\omega_2(\xi^2 + \omega_2^2)}. \tag{C.6}$$

$$y(t) = -\frac{e^{-\xi t}}{\xi} C_{1y} + C_{2y} - F_1 \frac{\xi \cos(\omega_1 t) + \omega_1 \sin(\omega_1 t)}{\omega_1(\xi^2 + \omega_1^2)} - F_2 \frac{\xi \cos(\omega_2 t) + \omega_2 \sin(\omega_2 t)}{\omega_2(\xi^2 + \omega_2^2)}. \tag{C.7}$$

The constants $C_{1x,y}$ and $C_{2x,y}$ are determined by the initial conditions of the system. The parameter ϕ is equal to zero for circular and inward flower patterns, and is equal to π for the outward flower patterns.

The values of both angular frequencies ω_1 and ω_2 and forcing amplitudes F_1 and F_2 can be directly determined from the spiral tip pattern of the spatially extended models. First, the frequencies are found explicitly from the Fourier power spectrum of the coordinates for the tip trajectory, as shown in Fig. C.1A. Second, explicit expressions for the forcing amplitudes can be derived by determining the maximum value, A_1, and minimum value, A_2, of $r = x^2 + y^2$, the spatial extent of the tip trajectory (see Fig. C.1B). This results in the following expressions for the forcing amplitudes:

$$F_1 = \frac{1}{2}\omega_1 (A_1 + A_2)\sqrt{\xi^2 + \omega_1^2} \tag{C.8}$$

$$F_2 = \omega_2 \sqrt{\xi^2 + \omega_2^2} \left(A_1 - \frac{F_1}{\omega_1 \sqrt{\xi^2 + \omega_1^2}} \right). \tag{C.9}$$

Resulting values for the SP model parameters are given in Table S3.

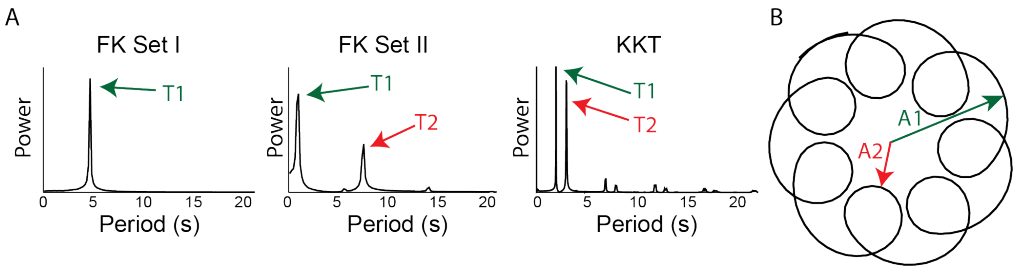

Figure C.1: A: Power spectrum of the x-component of the tip trajectory for the different electrophysiological models and parameter sets used in the main text. The spectra have either one or two peaks, corresponding to the frequencies $\omega_1 = 2\pi/T_1$ and $\omega_2 = 2\pi/T_2$. B: Diagram showing how A_1 and A_2 relate to the tip trajectory.

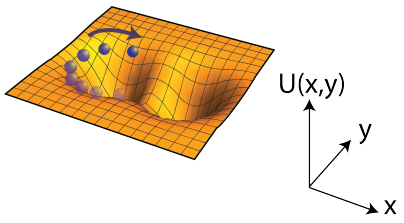

Figure C.2: Schematic representation of a particle moving in a potential landscape with two wells, representing tissue heterogeneities.

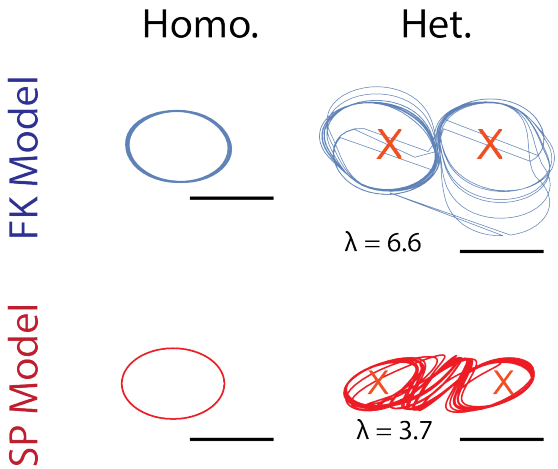

Figure C.3: Example trajectories with added anisotropy. The chaotic regime is still present in both models with heterogeneities. Anisotropy added to the FK model via the diffusion tensor, and the SP model by splitting the forcing terms F_i into F_{ix} and F_{2x}. All scale bars are 1cm.

Table C.1: Parameters used for the Fenton Karma model simulations as shown in the main text. All time constants τ are in milliseconds, all voltages are in rescaled, arbitrary units.

Parameter	Set I	Set II
τ_v^+	3.33	3.33
τ_{v1}^-	19.6	19.6
τ_{v2}^-	1000	1000
τ_w^+	50	50
τ_w^-	11	11
τ_d	0.43	0.403
τ_o	8.3	8.3
τ_r	50	50
τ_{si}	45	45
k	10	10
V_c^{si}	0.85	0.85
V_c	0.13	0.13
V_v	0.055	0.055
D	0.001	0.001

Table C.2: Parameters used for the KKT model simulations as shown in the main text. PNa was lowered to 0.001 nL/s in order to improve stability of the spiral wave.

Parameter	Value
$Na_o(mM)$	130.0
$Ca_o(mM)$	18.0
$K_o(mM)$	5.4
$C_m(nF)$	0.05
$B_{Na}(mM)$	1.132
$Kd_{BNa}(mM)$	10.0
$I_{NaKmax}(pA)$	70.0
$k_{NaKK}(mmol/L)$	1.0
$k_{NaKNa}(mmol/L)$	11.0
$B_{Ca}(mM)$	0.024
$Kd_{BCa}(mM)$	2.38E-03
$P_{Na}(nL/s)$	1.0E-03
$E_{Ca_app}(mV)$	60
kCa_n	2
$k_{Ca}(mM)$	6.00E-04
$I_{CaPmax}(pA)$	2
$k_{CaP}(mM)$	5.00E-04
γ	0.45
$d_{NaCa}(mmol/L)^{-4}$	3.00E-04
$D_{Ca}(\mu m^2/s)$	780
$D_{CaSR}(\mu m^2/s)$	44
$D_{CaBm}(\mu m^2/s)$	25
$D_{Na}(\mu m^2/s)$	0.12
$k_4(s^{-1})$	13
$k_{SRleak}(s^{-1})$	6.00E-03
$CSQN(mM)$	6.7
$Kd_{CSQN}(mM)$	0.8
$k_{NaCa}(pA/(mmol/L)^4)$	0.0084
$g_{Ks}(nS)$	1
$g_{K1}(nS)$	3.45
$g_{Nab}(nS)$	0.0606
$g_{Cab}(nS)$	0.0952
$g_{If}(nS)$	1.0
$g_{CaL}(nS)$	15.0
$g_t(nS)$	8.25
$g_{sus}(nS)$	2.25
$g_{Kr}(nS)$	0.50
$SLlow(mM)$	165.0
$SLhigh(mM)$	13.0
$Kd_{SLlow}(mM)$	1.10
$Kd_{SLhigh}(mM)$	13E-3
$D(cm^2/ms)$	1.00E-03

Table C.3: The parameters for the SP model that reproduce the homogeneous patterns of Set I, Set II, and the KKT model in the main text. The forcing terms F_1 and F_2 can be found from A_1 and A_2 using the equations given above. The value of ϕ is set to 0 for both FK sets, and π for the KKT set.

Pattern	$\xi(1/ms)$	$F_1(cm/ms^2)$	$F_2(cm/ms^2)$	$A_1(cm)$	$A_2(cm)$	$T_1(ms)$	$T_2(ms)$
FK(Set I)	0.05	0.001	0.0	0.625	0.625	214	-
FK(Set II)	0.05	2.1E-4	1.1E-3	1.075	0.347	1080	137
KKT	0.05	5.4E-4	7.2E-4	1.574	0.1374	518	335

Bibliography

[ABE16] Sergio Alonso, Markus Br, and Blas Echebarria. Nonlinear physics of electrical wave propagation in the heart: a review. *Reports on Progress in Physics*, 79(9):096601, 2016.

[Ant07] Charles Antzelevitch. Heterogeneity and cardiac arrhythmias: an overview. *Heart Rhythm*, 4(7):964–972, 2007.

[Bar94] Dwight Barkley. Euclidean symmetry and the dynamics of rotating spiral waves. *Phys. Rev. Lett.*, 72:164–167, Jan 1994.

[BB03] I. V. Biktasheva and V. N. Biktashev. Wave-particle dualism of spiral waves dynamics. *Phys. Rev. E*, 67:026221, Feb 2003.

[BBPL17] Philip Bittihn, Sebastian Berg, Ulrich Parlitz, and Stefan Luther. Emergent dynamics of spatio-temporal chaos in a heterogeneous excitable medium. *Chaos: An Interdisciplinary Journal of Nonlinear Science*, 27(9):093931, 2017.

[BCG$^+$] Ezio Bartocci, Elizabeth M Cherry, James Glimm, Radu Grosu, Scott A Smolka, and Flavio H Fenton. Toward real-time simulation of cardiac dynamics. In *Proceedings of the 9th International Conference on Computational Methods in Systems Biology*, pages 103–112. ACM.

[BKO$^+$12] Corina T Bot, Armen R Kherlopian, Francis A Ortega, David J Christini, and Trine Krogh-Madsen. Rapid genetic algorithm optimization of a mouse computational model: benefits for anthropomorphization of neonatal mouse cardiomyocytes. *Frontiers in physiology*, 3, 2012.

[BOCF08] A. Bueno-Orovio, E. M. Cherry, and F. H. Fenton. Minimal model for human ventricular action potentials in tissue. *J. Theor. Biol.*, 253(3):544–560, 2008.

[BS03a] Kevin S Brown and James P Sethna. Statistical mechanical approaches to models with many poorly known parameters. *Physical Review E*, 68(2):021904, 2003.

[BS03b] Kevin S. Brown and James P. Sethna. Statistical mechanical approaches to models with many poorly known parameters. *Phys. Rev. E*, 68:021904, Aug 2003.

[CBBH01] R. H. Clayton, A. Bailey, V. N. Biktashev, and A. V. Holden. Re-entrant cardiac arrhythmias in computational models of long QT myocardium. *J Theor Biol*, 208:215–225, 2001.

[CBC+11] R. H. Clayton, O. Bernus, E. M. Cherry, H. Dierckx, F. H. Fenton, L. Mirabella, A. V. Panfilov, F. B. Sachse, G. Seemann, and H. Zhang. Models of cardiac tissue electrophysiology: progress, challenges and open questions. *Prog Biophys Mol Biol*, 104(1-3):22–48, 2011.

[CCY+12] F. Chen, A. Chu, X. Yang, Y. Lei, and J. Chu. Identification of the parameters of the beeler-reuter ionic equation with a partially perturbed particle swarm optimization. *IEEE Trans Biomed Eng*, 59(12):3412–21, 2012.

[CE08] E. M. Cherry and S.J. Evans. Properties of two human atrial cell models in tissue: restitution, memory, propagation, and reentry. *J Theor Biol*, 254:674–690, 2008.

[CENF07] E. M. Cherry, J. R. Ehrlich, S. Nattel, and F. H. Fenton. Pulmonary vein reentry–properties and size matter: insights from a computational analysis. *Heart Rhythm*, 4(12):1553–62, 2007.

[CF07] E. M. Cherry and F. H. Fenton. A tale of two dogs: analyzing two models of canine ventricular electrophysiology. *Am J Physiol Heart Circ Physiol*, 292(1):H43–55, 2007.

[CF08] E. M. Cherry and F. H. Fenton. Visualization of spiral and scroll waves in simulated and experimental cardiac tissue. *New J. Phys*, 10:125016, 2008.

[CF11] E. M. Cherry and F. H. Fenton. Effects of boundaries and geometry on the spatial distribution of action potential duration in cardiac tissue. *J Theor Biol*, 285(1):164–76, 2011.

[CHA95] TERESA REE CHAY. Bifurcations in heart rhythms. *International Journal of Bifurcation and Chaos*, 05(06):1439–1486, 1995.

[CHN+13] Sumeet S Chugh, Rasmus Havmoeller, Kumar Narayanan, David Singh, Michiel Rienstra, Emelia J Benjamin, Richard F Gillum, Young-Hoon Kim, John H McAnulty, Zhi-Jie Zheng, et al. Worldwide epidemiology of atrial fibrillation: a global burden of disease 2010 study. *Circulation*, pages CIRCULATIONAHA–113, 2013.

[CRN98] M. Courtemanche, R. J. Ramirez, and S. Nattel. Ionic mechanisms underlying human atrial action potential properties: insights from a mathematical model. *Am J Physiol*, 275(1 Pt 2):H301–H321, 1998.

[DDP13] Arne Defauw, Peter Dawyndt, and Alexander V Panfilov. Initiation and dynamics of a spiral wave around an ionic heterogeneity in a model for human cardiac tissue. *Physical Review E*, 88(6):062703, 2013.

[DL04] S. Dokos and N. H. Lovell. Parameter estimation in cardiac ionic models. *Prog Biophys Mol Biol*, 85(2-3):407–31, 2004.

[ES96] Irving R Epstein and Kenneth Showalter. Nonlinear chemical dynamics: oscillations, patterns, and chaos. *The Journal of Physical Chemistry*, 100(31):13132–13147, 1996.

[FCHE02] F. H. Fenton, E. M. Cherry, H. M. Hastings, and S. J. Evans. Multiple mechanisms of spiral wave breakup in a model of cardiac electrical activity. *Chaos*, 12:852–892, 2002.

[FCKR05] F. H. Fenton, E. M. Cherry, A. Karma, and W.-J. Rappel. Modeling wave propagation in realistic heart geometries using the phase-field method. *Chaos*, 15(1):13502, 2005.

[FEH99] Flavio H Fenton, Steven J Evans, and Harold M Hastings. Memory in an excitable medium: a mechanism for spiral wave breakup in the low-excitability limit. *Physical review letters*, 83(19):3964, 1999.

[FK98] F. Fenton and A. Karma. Vortex dynamics in three-dimensional continuous myocardium with fiber rotation: Filament instability and fibrillation. *Chaos*, 8:20–47, 1998.

[FKFZ95] M. R. Franz, P. F. Kirchhof, C. L. Fabritz, and M. Zabel. Computer analysis of monophasic action potentials: manual validation and clinically pertinent applications. *Pacing Clin Electrophysiol*, 18(9 Pt 1):1666–1678, 1995.

[FNC+11] Martin Fink, Steven A Niederer, Elizabeth M Cherry, Flavio H Fenton, Jussi T Koivumäki, Gunnar Seemann, Rüdiger Thul, Henggui Zhang, Frank B Sachse, Dan Beard, et al. Cardiac cell modelling: observations from the heart of the cardiac physiome project. *Progress in biophysics and molecular biology*, 104(1):2–21, 2011.

[GB83] NA Gorelova and J Bureš. Spiral waves of spreading depression in the isolated chicken retina. *Developmental Neurobiology*, 14(5):353–363, 1983.

[GBR+72] H. Gelband, H. L. Bush, M. R. Rosen, R. J. Myerburg, and B. F. Hoffman. Electrophysiologic properties of isolated preparations of human atrial myocardium. *Circ Res*, 30(3):293–300, 1972.

[GEKS92] Charles M Gray, Andreas K Engel, Peter König, and Wolf Singer. Synchronization of oscillatory neuronal responses in cat striate cortex: temporal properties. *Visual neuroscience*, 8(04):337–347, 1992.

[GPJ98] R.A. Gray, A.M. Pertsov, and J. Jalife. Spatial and temporal organization during cardiac fibrillation. *Nature*, 392(6671):75–78, 1998.

[GPV+11] E. Grandi, S. V. Pandit, N. Voigt, A. J. Workman, D. Dobrev, J. Jalife, and D. M. Bers. Human atrial action potential and Ca2+ model: sinus rhythm and chronic atrial fibrillation. *Circ. Res.*, 109(9):1055–1066, 2011.

[GSK+13] M. J. Gonzales, G. Sturgeon, A. Krishnamurthy, J. Hake, R. Jonas, P. Stark, W.-J. Rappel, S. M. Narayan, Y. Zhang, W. P. Segars, and A. D. McCulloch. A three-dimensional finite element model of human atrial anatomy: new methods for cubic Hermite meshes with extraordinary vertices. *Med Image Anal*, 17(5):525–537, 2013.

[GVR+14] M. J. Gonzales, K. P. Vincent, W.-J. Rappel, S. M. Narayan, and A. D. McCulloch. Structural contributions to fibrillatory rotors in a patient-derived computational model of the atria. *Europace*, 16 Suppl 4:iv3–iv10, 2014.

[GWC+07] Ryan N Gutenkunst, Joshua J Waterfall, Fergal P Casey, Kevin S Brown, Christopher R Myers, and James P Sethna. Universally sloppy parameter sensitivities in systems biology models. *PLoS Comput Biol*, 3(10):e189, 2007.

[GXS+07] Y. Gong, F. Xie, K. M. Stein, A. Garfinkel, C. A. Culianu, B. B. Lerman, and D. J. Christini. Mechanism underlying initiation of paroxysmal atrial flutter/atrial fibrillation by ectopic foci: a simulation study. *Circulation*, 115(16):2094–102, 2007.

[HHD+14] M. Haissaguerre, M. Hocini, A. Denis, A. J. Shah, Y. Komatsu, S. Yamashita, M. Daly, S. Amraoui, S. Zellerhoff, M. Q. Picat, A. Quotb, L. Jesel, H. Lim, S. Ploux, P. Bordachar, G. Attuel, V. Meillet, P. Ritter, N. Derval, F. Sacher, O. Bernus, H. Cochet, P. Jais, and R. Dubois. Driver domains in persistent atrial fibrillation. *Circulation*, 130(7):530–538, 2014.

[HSC+16] Michel Haissaguerre, Ashok J Shah, Hubert Cochet, Meleze Hocini, Remi Dubois, Igor Efimov, Edward Vigmond, Olivier Bernus, and Natalia Trayanova. Intermittent drivers anchoring to structural heterogeneities as a major pathophysiological mechanism of human persistent atrial fibrillation. *The Journal of physiology*, 594(9):2387–2398, 2016.

[HVND14] J. Heijman, N. Voigt, S. Nattel, and D. Dobrev. Cellular and molecular electrophysiology of atrial fibrillation initiation, maintenance, and progression. *Circ Res*, 114(9):1483–99, 2014.

[Jal11] J. Jalife. Deja vu in the theories of atrial fibrillation dynamics. *Cardiovasc Res*, 89(4):766–75, 2011.

[JRE+90] S Jakubith, HH Rotermund, W Engel, A Von Oertzen, and G Ertl. Spatiotemporal concentration patterns in a surface reaction: Propagating and standing waves, rotating spirals, and turbulence. *Physical Review Letters*, 65(24):3013, 1990.

[Kar94] A. Karma. Electrical alternans and spiral wave breakup in cardiac tissue. *Chaos*, 4(3):461–472, 1994.

[Kar13] Alain Karma. Physics of cardiac arrhythmogenesis. *Annu. Rev. Condens. Matter Phys.*, 4(1):313–337, 2013.

[KDT+04] Soma S Kalb, Hana M Dobrovolny, Elena G Tolkacheva, Salim F Idriss, Wanda Krassowska, and Daniel J Gauthier. The restitution portrait. *Journal of cardiovascular electrophysiology*, 15(6):698–709, 2004.

[KKB+91] Boris Y Kogan, Walter J Karplus, Brian S Billett, Alex T Pang, Hrayr S Karagueuzian, and Steven S Khan. The simplified fitzhugh-nagumo model with action potential duration restitution: effects on 2d wave propagation. *Physica D: Nonlinear Phenomena*, 50(3):327–340, 1991.

[KKT11] J. T. Koivumaki, T. Korhonen, and P. Tavi. Impact of sarcoplasmic reticulum calcium release on calcium dynamics and action potential morphology in human atrial myocytes: a computational study. *PLoS Comput. Biol.*, 7(1):e1001067, 2011.

[KOC11] Armen R Kherlopian, Francis A Ortega, and David J Christini. Cardiac myocyte model parameter sensitivity analysis and model transformation using a genetic algorithm. In *Proceedings of the 13th annual conference companion on Genetic and evolutionary computation*, pages 755–758. ACM, 2011.

[KSMT14] J. T. Koivumaki, G. Seemann, M. M. Maleckar, and P. Tavi. In silico screening of the key cellular remodeling targets in chronic atrial fibrillation. *PLoS Comput. Biol.*, 10(5):e1003620, 2014.

[LB13] Jacob Langham and Dwight Barkley. Non-specular reflections in a macroscopic system with wave-particle duality: Spiral waves in bounded media. *Chaos: An Interdisciplinary Journal of Nonlinear Science*, 23(1):013134, 2013.

[LCG96] Kyoung J Lee, Edward C Cox, and Raymond E Goldstein. Competing patterns of signaling activity in dictyostelium discoideum. *Physical review letters*, 76(7):1174, 1996.

[LFNR16] Daniel M Lombardo, Flavio H Fenton, Sanjiv M Narayan, and Wouter-Jan Rappel. Comparison of detailed and simplified models of human atrial myocytes to recapitulate patient specific properties. *PLoS Comput Biol*, 12(8):e1005060, 2016.

[LR17] Daniel M Lombardo and Wouter-Jan Rappel. Systematic reduction of a detailed atrial myocyte model. *Chaos: An Interdisciplinary Journal of Nonlinear Science*, 27(9):093914, 2017.

[LSG+12] G. G. Lalani, A. Schricker, M. Gibson, A. Rostamian, D. E. Krummen, and S. M. Narayan. Atrial conduction slows immediately before the onset of human atrial

fibrillation: a bi-atrial contact mapping study of transitions to atrial fibrillation. *J Am Coll Cardiol*, 59(6):595–606, 2012.

[MGTG08] M. M. Maleckar, J. L. Greenstein, N. A. Trayanova, and W. R. Giles. Mathematical simulations of ligand-gated and cell-type specific effects on the action potential of human atrium. *Prog. Biophys. Mol. Biol.*, 98(2-3):161–170, 2008.

[MVB+12] Kathleen S McDowell, Fijoy Vadakkumpadan, Robert Blake, Joshua Blauer, Gernot Plank, Rob S MacLeod, and Natalia A Trayanova. Methodology for patient-specific modeling of atrial fibrosis as a substrate for atrial fibrillation. *Journal of electrocardiology*, 45(6):640–645, 2012.

[MVB+13] K. S. McDowell, F. Vadakkumpadan, R. Blake, J. Blauer, G. Plank, R. S. Macleod, and N. A. Trayanova. Mechanistic inquiry into the role of tissue remodeling in fibrotic lesions in human atrial fibrillation. *Biophys J*, 104(12):2764–73, 2013.

[Nat02] S. Nattel. New ideas about atrial fibrillation 50 years on. *Nature*, 415(6868):219–26, 2002.

[NFC+11] Sanjiv M Narayan, Michael R Franz, Paul Clopton, Etienne J Pruvot, and David E Krummen. Repolarization alternans reveals vulnerability to human atrial fibrillationclinical perspective. *Circulation*, 123(25):2922–2930, 2011.

[NFF+98] A. Nygren, C. Fiset, L. Firek, J. W. Clark, D. S. Lindblad, R. B. Clark, and W. R. Giles. Mathematical model of an adult human atrial cell: the role of K+ currents in repolarization. *Circ Res*, 82(1):63–81, 1998.

[NFNS09] S. A. Niederer, M. Fink, D. Noble, and N. P. Smith. A meta-analysis of cardiac electrophysiology computational models. *Exp Physiol*, 94(5):486–95, 2009.

[NKER12] S. M. Narayan, D. E. Krummen, M. W. Enyeart, and W.-J. Rappel. Computational mapping identifies localized mechanisms for ablation of atrial fibrillation. *PLoS ONE*, 7(9):e46034, 2012.

[NKKR08] S. M. Narayan, D. Kazi, D. E. Krummen, and W. J. Rappel. Repolarization and activation restitution near human pulmonary veins and atrial fibrillation initiation: a mechanism for the initiation of atrial fibrillation by premature beats. *J Am Coll Cardiol*, 52(15):1222–30, 2008.

[NKR12] Sanjiv M Narayan, David E Krummen, and Wouter-Jan Rappel. Clinical mapping approach to diagnose electrical rotors and focal impulse sources for human atrial fibrillation. *Journal of cardiovascular electrophysiology*, 23(5):447–454, 2012.

[NKS+12] Sanjiv M Narayan, David E Krummen, Kalyanam Shivkumar, Paul Clopton, Wouter-Jan Rappel, and John M Miller. Treatment of atrial fibrillation by the ablation of localized sourcesconfirm (conventional ablation for atrial fibrillation with or without

focal impulse and rotor modulation) trial. *Journal of the American College of Cardiology*, 60(7):628–636, 2012.

[Nob] D. Noble. A modification of the hodgkinhuxley equations applicable to purkinje fibre action and pacemaker potentials. *The Journal of Physiology*, 160(2):317–352.

[OBK+09a] R. S. Oakes, T. J. Badger, E. G. Kholmovski, N. Akoum, N. S. Burgon, E. N. Fish, J. J. Blauer, S. N. Rao, E. V. DiBella, N. M. Segerson, M. Daccarett, J. Windfelder, C. J. McGann, D. Parker, R. S. MacLeod, and N. F. Marrouche. Detection and quantification of left atrial structural remodeling with delayed-enhancement magnetic resonance imaging in patients with atrial fibrillation. *Circulation*, 119(13):1758–67, 2009.

[OBK+09b] Robert S Oakes, Troy J Badger, Eugene G Kholmovski, Nazem Akoum, Nathan S Burgon, Eric N Fish, Joshua JE Blauer, Swati N Rao, Edward VR DiBella, Nathan M Segerson, et al. Detection and quantification of left atrial structural remodeling with delayed-enhancement magnetic resonance imaging in patients with atrial fibrillation. *Circulation*, 119(13):1758–1767, 2009.

[Olm10] Daniel Olmos. Reflection and attachment of spirals at obstacles for the fitzhugh-nagumo and beeler-reuter models. *Physical Review E*, 81(4):041924, 2010.

[PB88] R. Plonsey and R.C. Barr. *Bioelectricity: a quantitative approach*. Plenum Press, New York, 1988.

[PTVF07] William H. Press, Saul A. Teukolsky, William T. Vetterling, and Brian P. Flannery. *Numerical Recipes 3rd Edition: The Art of Scientific Computing*. Cambridge University Press, 2007.

[QWG00] Zhilin Qu, James N Weiss, and Alan Garfinkel. From local to global spatiotemporal chaos in a cardiac tissue model. *Physical Review E*, 61(1):727, 2000.

[QXGW00] Z. Qu, F. Xie, A. Garfinkel, and J. N. Weiss. Origins of spiral wave meander and breakup in a two-dimensional cardiac tissue model. *Ann Biomed Eng*, 28(7):755–771, 2000.

[Rap01] W.-J. Rappel. Filament instability and rotational tissue anisotropy: A numerical study using detailed cardiac models. *Chaos*, 11:71–80, 2001.

[SCBF+13] E. P. Scholz, P. Carrillo-Bustamante, F. Fischer, M. Wilhelms, E. Zitron, O. Dossel, H. A. Katus, and G. Seemann. Rotor termination is critically dependent on kinetic properties of i kur inhibitors in an in silico model of chronic atrial fibrillation. *PLoS One*, 8(12):e83179, 2013.

[Sil52] Weidmann Silvio. The electrical constants of purkinje fibres. *The Journal of Physiology*, 118:348–60, 1952.

[SLR12] D. Shao, H. Levine, and W. J. Rappel. Coupling actin flow, adhesion, and morphology in a computational cell motility model. *Proc Natl Acad Sci U S A*, 109(18):6851–6, 2012.

[SVNL05] Z. Syed, E. Vigmond, S. Nattel, and L. J. Leon. Atrial cell action potential parameter fitting using genetic algorithms. *Med Biol Eng Comput*, 43(5):561–71, 2005.

[SYE+14] M. Skoge, H. Yue, M. Erickstad, A. Bae, H. Levine, A. Groisman, W. F. Loomis, and W. J. Rappel. Cellular memory in eukaryotic chemotaxis. *Proc Natl Acad Sci U S A*, 111(40):14448–53, 2014.

[Tho56a] William Thomson. Iii. on the theory of the electric telegraph. *Proceedings of the Royal Society of London*, 7:382–399, 1856.

[Tho56b] William Thomson. On peristaltic induction of electric currents. *Proceedings of the Royal Society of London*, 8:121–132, 1856.

[TMS10] Mark K. Transtrum, Benjamin B. Machta, and James P. Sethna. Why are nonlinear fits to data so challenging? *Phys. Rev. Lett.*, 104:060201, Feb 2010.

[TMS11] Mark K. Transtrum, Benjamin B. Machta, and James P. Sethna. Geometry of nonlinear least squares with applications to sloppy models and optimization. *Phys. Rev. E*, 83:036701, Mar 2011.

[TQ14] Mark K. Transtrum and Peng Qiu. Model reduction by manifold boundaries. *Phys. Rev. Lett.*, 113:098701, Aug 2014.

[Tra14] Natalia A Trayanova. Your personal virtual heart. *IEEE Spectrum*, 51(11):34–59, 2014.

[TS12] Mark K. Transtrum and James P. Sethna. Improvements to the Levenberg-Marquardt algorithm for nonlinear least-squares minimization, 2012. arXiv:1201.5885v1.

[TSA+12] K. Takeda, D. Shao, M. Adler, P. G. Charest, W. F. Loomis, H. Levine, A. Groisman, W. J. Rappel, and R. A. Firtel. Incoherent feedforward control governs adaptation of activated ras in a eukaryotic chemotaxis pathway. *Sci Signal*, 5(205):ra2, 2012.

[tTP06] Kirsten HWJ ten Tusscher and Alexander V Panfilov. Alternans and spiral breakup in a human ventricular tissue model. *American Journal of Physiology-Heart and Circulatory Physiology*, 291(3):H1088–H1100, 2006.

[VJH+02] Nathalie Virag, Vincent Jacquemet, CS Henriquez, Steeve Zozor, Olivier Blanc, J-M Vesin, Etienne Pruvot, and Lukas Kappenberger. Study of atrial arrhythmias in a computer model based on magnetic resonance images of human atria. *Chaos: An Interdisciplinary Journal of Nonlinear Science*, 12(3):754–763, 2002.

[VRT+09] F. Vadakkumpadan, L. J. Rantner, B. Tice, P. Boyle, A. J. Prassl, E. Vigmond, G. Plank, and N. Trayanova. Image-based models of cardiac structure with applications in arrhythmia and defibrillation studies. *J Electrocardiol*, 42(2):157 e1–10, 2009.

[WHM+12] M. Wilhelms, H. Hettmann, M. M. Maleckar, J. T. Koivumaki, O. Dossel, and G. Seemann. Benchmarking electrophysiological models of human atrial myocytes. *Front Physiol*, 3:487, 2012.

[Win72] Arthur T Winfree. Spiral waves of chemical activity. *Science*, 175(4022):634–636, 1972.

[Win91] Arthur T Winfree. Varieties of spiral wave behavior: An experimentalists approach to the theory of excitable media. *Chaos: An Interdisciplinary Journal of Nonlinear Science*, 1(3):303–334, 1991.

[WIT08] Seth Weinberg, Shahriar Iravanian, and Leslie Tung. Representation of collective electrical behavior of cardiac cell sheets. *Biophysical Journal*, 95(3):1138 – 1150, 2008.

[WMR+12] A. J. Workman, G. E. Marshall, A. C. Rankin, G. L. Smith, and J. Dempster. Transient outward K+ current reduction prolongs action potentials and promotes afterdepolarisations: a dynamic-clamp study in human and rabbit cardiac atrial myocytes. *J. Physiol. (Lond.)*, 590(Pt 17):4289–4305, 2012.

[WNGQ11] J. N. Weiss, M. Nivala, A. Garfinkel, and Z. Qu. Alternans and arrhythmias: from cell to heart. *Circ Res*, 108(1):98–112, 2011.

[WSSV85] Alan Wolf, Jack B. Swift, Harry L. Swinney, and John A. Vastano. Determining lyapunov exponents from a time series. *Physica D: Nonlinear Phenomena*, 16(3):285 – 317, 1985.

[XLQD12] L Xu, Z Li, Z Qu, and Z Di. Resonance drifts of spiral waves on media of periodic excitability. *Physical Review. E, Statistical, Nonlinear, and Soft Matter Physics*, 2012.

[XQG98] Fagen Xie, Zhilin Qu, and Alan Garfinkel. Dynamics of reentry around a circular obstacle in cardiac tissue. *Physical Review E*, 58(5):6355, 1998.

[ZBLC+14] Massimo Zoni-Berisso, Fabrizio Lercari, Tiziana Carazza, Stefano Domenicucci, et al. Epidemiology of atrial fibrillation: European perspective. *Clin Epidemiol*, 6(213):e220, 2014.

[ZH95] H. Zhang and A.V. Holden. Chaotic meander of spiral waves in the fitzhugh-nagumo system. *Chaos, Solitons & Fractals*, 5(3):661 – 670, 1995. Nonlinear Phenomena in Excitable Physiological Systems.

[ZKB17] Vladimir Zykov, Alexei Krekhov, and Eberhard Bodenschatz. Fast propagation regions cause self-sustained reentry in excitable media. *Proceedings of the National Academy of Sciences*, 114(6):1281–1286, 2017.

[ZLK93] Xiaoqin Zou, Herbert Levine, and David A Kessler. Interaction between a drifting spiral and defects. *Physical Review E*, 47(2):R800, 1993.

[ZP12] Christian W Zemlin and Arkady M Pertsov. Anchoring of drifting spiral and scroll waves to impermeable inclusions in excitable media. *Physical review letters*, 109(3):038303, 2012.